Optimization of RF-induced Breakdown of Plasma on the QUEST Spherical Tokamak

米田, 亮太

https://doi.org/10.15017/1931947

出版情報：九州大学, 2017, 博士（工学）, 課程博士
バージョン：
権利関係：

Doctoral Thesis

Optimization of RF-induced Breakdown of Plasma on the QUEST Spherical Tokamak

ASEM, IGSES, Kyushu University
Ryota YONEDA

Contents

1. Introduction

In 21th century, multi-polarity of the world economy arises such as BRICs (Brazil, Russia, India and China) or developing countries in Asia and Africa. A huge consumption of energy resources has been a critical issue to realize sustainable development under the conditions that not only for inhibiting the global warming but also constraining energy resources such as petroleum and water. This situation requires an intensive international cooperation in many aspects. In nuclear fusion research and technology development, as an ultimate solution for energy crisis, we have been pursuing the realization of fusion-based power plant in worldwide collaborations.

1.1 Nuclear Fusion Energy

The nuclear fusion energy is quite different from the technology used in the current nuclear power plants. It should be noted briefly how it works to avoid misunderstandings. The principle used in general nuclear power plant is called nuclear fission. In fission power, we use Uranium 235. As a neutron hits Uranium, its nucleus separated into two nucleuses. When this reaction occurs there exists a difference in total mass between before and after the reaction. This difference of total mass is released as energy following the famous equation by Einstein ($E=mc^2$). The fission reaction also produces few neutrons and they hit other Uranium. By discreet controlling of reactions under the operational range enables a continuous production of energy. Fission requires careful control to prevent runaway of reactor. In contrast, nuclear fusion uses light atoms such as deuterium and tritium (they are the isotopes of hydrogen). In the reaction between deuterium and tritium (D-T reaction) in Fig. 1-1, it produces helium atom and one neutron. There is also a mass difference before and after, which is equivalent to the energy released. The concept of fusion power plant is the utilization of this fusion reaction.

The uniqueness of nuclear fusion energy basically can be described as following[1]: (1) The deuterium as fuel exists 1cc within 3L of usual water. Therefore, there is no resource shortage for nuclear fusion. (2) It produces no waste that contaminates environment such as CO2 and there is no requirement of material treatment for ultra-long term. (3) The nuclear fusion reaction at the reactor core can be controlled safely. These three points are often mentioned when making a comparison with nuclear fission. Therefore, let us consider more in detail here. For (1), power generation output of 100 million kW with D-T reaction requires 200g of deuterium per day. 150 ppm of hydrogen isotope within whole amount of water in the ocean is deuterium, therefore can say deuterium deposit is inexhaustible.

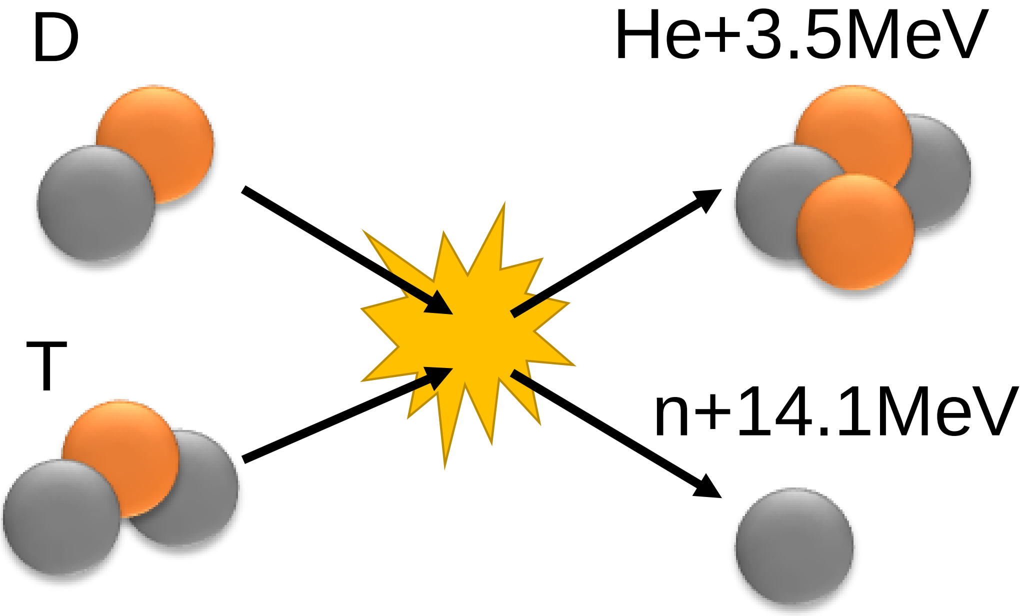

Fig. 1-1. D-T fusion reaction diagram.

The question is how to separate it from water practically. There is a misunderstanding that the separation of water by electrolysis takes huge amount of energy and this makes fusion impossible to generate net of energy at all. It is true that to divide water by electrolysis and proceed isotope separation consume great deal of energy, however, water molecular itself has a slight difference in chemical property whether it contains normal hydrogen or deuterium. Making use of this difference, it is possible to separate deuterium efficiently. Plants for the deuterium separation already exist all over the world. Especially, in Canada, it has been well-developed and commercialized. For (2), one should mention that radioactive materials can be produced during the operation of fusion reactor. Tritium as fuel is radioactive and it is also almost non-existent in nature. Therefore, it can be produced by nuclear reactions between lithium and neutrons from fusion reaction inside the blanket. The blanket is a device located inside of fusion reactor that contains lithium to produce tritium and inject it as fuel into fusion plasma. The point is that only few percent of the injected fuels (deuterium and tritium) can make fusion reaction so that the rest would be released as exhaust emission. Tritium has mobility and it must be carefully handled. Another radioactive material can be also produced that energetic neutrons from fusion plasma make plasma facing components radioactive. This kind of radioactive is solid state and low level that it is relatively easy to handle compared with radioactive from fission power reactor. Technology for the blanket has been a key issue and intensively studied. Finally, about (3), we see the reason why there is no runaway with fusion reactor. In magnetic confinement of fusion plasma, the possible operation range for fusion reaction is very narrow. Such required temperature and density of plasma are sensitive for fuel injection or impurities. If there is an error in operation such as excess supply of fuel, it cannot sustain the reaction conditions. Then, it terminates automatically. Of course, a sudden termination can cause damage to the reactor so that safe operation is also of importance[2]. In these manner, nuclear fusion energy is not perfectly clean. Even though, the amount of energy that it can produce would be enormous. As one alternative, nuclear fusion should be taken account.

What makes fusion so difficult? It will be also mentioned in next section that for fusion reaction both high performance plasma and high confinement of plasma are required[3]. These conditions are against each other, such high-performance plasma with high temperature and density tries to escape from confinement area. For this purpose, a large construction of fusion device is needed to sustain fusion reaction by applying large amplitude of magnetic field. Note that for D-T reaction, temperature more than 100 million Celsius is necessary (see Fig. 1-2).

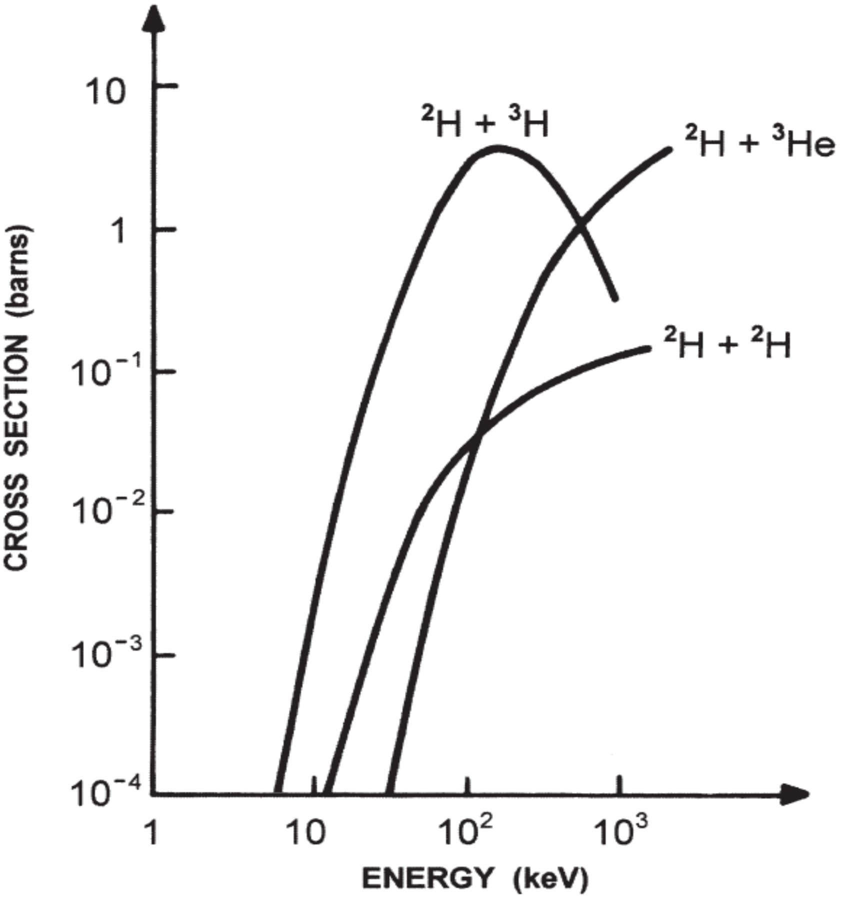

Fig. 1-2. Fusion cross sections, in barns (1 barn = 10^{-28}m^2) as a function of center of mass energy (keV).

There are mainly 11 technical considerations for realizing a fusion tokamak reactor: superconducting coils, blanket, divertor, plasma heating & current drive, physics & simulation, core plasma physics, fusion fuel system, materials of reactor, reactor safety design, occupancy rate & maintainability and measurement & control[4]. Here, brief explanations for some terminologies are given. First, superconducting coil is a specialized coil that can produce strong magnetic field. The superconducting condition makes metal materials no electrical resistance that high current can generate much higher magnetic field. For this condition, extreme cooling of coil is necessary. Therefore, separation between hot plasma and superconducting coils are to be realized. This poses technical difficulties and a large complex construction is indispensable. Second, divertor is a part of tokamak that exhaust helium or impurities from reaction to sustain long-duration tokamak operation. It is also the area where the strongest heat load comes due to magnetic field configuration. Since the expected heat load in fusion reactor would be 10 MW per m^{-2}, which is an order of magnitude larger than fission reactor. Maintainability of reactor should be also mentioned. In a fusion power plant, materials and equipment inside the reactor are to be radioactivated by energetic neutrons from fusion reaction. Maintenance by human will be impossible so that remote maintenance by machines are planned.

1.2 Tokamak Reactor Concept

Tokamak is the most developed fusion reactor. It originally comes from a Russian term meaning “toroidal magnetic container”.[5] Tokamak consists of two superposition of two divided magnetic fields, a toroidal field (TF) and a poloidal field (PF) (see Fig. 1-3). Toroidal field is induced by currents flowing through external coil windings. Poloidal field can be generated by toroidal currents of confined plasma itself. The uniqueness of tokamak lies in this application of toroidal current. A simple toroidal magnetic configuration cannot hold plasma since ions and electrons drift in different vertical directions (gradient B drift). The induced electric field by this charge separation brings out $E \times B$ drift that plasma runs away rapidly in the radial direction. By driving toroidal current, the generated poloidal magnetic field cancel out the charge separation forming helical shaped magnetic lines of force. Then, we also apply poloidal field by PF coils located outside of vessel to push back plasma since they try to escape outward with hoop force. In conventional tokamak, the toroidal current (or plasma current) is induced by solenoid located at the center of the torus and often referred as center solenoid (CS). This CS is also used to initiate plasma (breakdown of plasma) and this initiation method is called inductive (or Ohmic) breakdown. Plasma current produced by CS is temporal because we cannot keep altering the coil current for such a long time and also as plasma temperature goes higher, frictions between plasma particles are hardly obtained. This poses a limitation of Joule heating and requires other technique of heating (auxiliary heating). The main ways to provide this auxiliary heating are Neutral Beam Injection (NBI) and Radio Frequency (RF) wave injection.

Intensive research on tokamak plasmas has been demonstrated for realization of fusion power plant since 1960's in T-3[6], JFT-2[7], Alcator[8], DITE[9], ASDEX[10], Tore Supra[11] and so on. T-3 firstly showed that tokamak configuration can confine plasma temperature of 1keV and this is the beginning tokamak research had rapidly spread all over the world. In 1990's, power output in the order of MW from D-T reactions were obtained in JET[12] and TFTR[13]. In JT-60U[14], high quality plasmas were made by D and its peak fusion amplification factor would be in excess of unity if deuterium-tritium fuel was used.

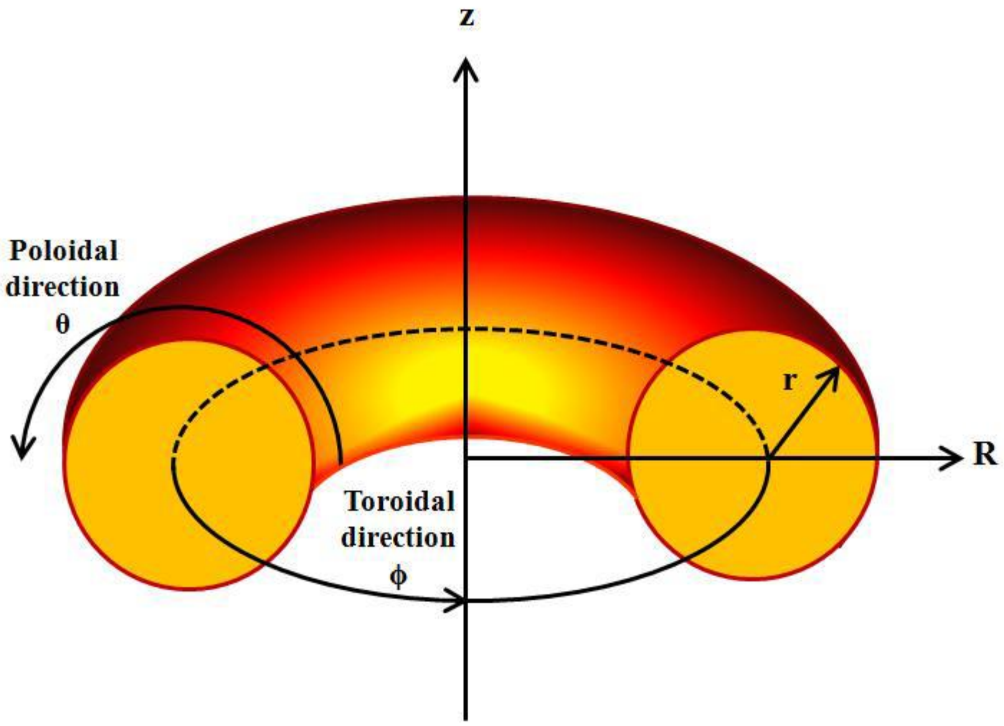

Fig. 1-3. Tokamak type of magnetic configuration for confinement of plasma.

1.3 Spherical Tokamak

In this section, the uniqueness of spherical tokamak will be discussed. The aspect ratio is defined as $A = R_0/a$, where R_0 is major radius and a is minor radius of the torus. When the ratio is under 1.5, the sectional view of tokamak becomes D-shaped and the appearance turns up spherical. Tokamaks with this feature are called 'spherical tokamak (ST)'. Comparison of conventional and spherical tokamak is illustrated in Fig. 1-4.

The most noteworthy advantage of ST is its stability with high-β. β is defined as the ratio of plasma pressure against magnetic pressure. Usually, the volume average of plasma pressure, <p> and the pressure of toroidal magnetic field at $R = R_0$, $B_{t0}^2/(2\mu_0)$ are used. The characteristic of high-β plasma is that we can achieve the same scale of nuclear reactor with lower toroidal magnetic field. During the construction of tokamak reactor, TF system occupies most of the cost. This is the reason why ST is said cost-effective and has been getting significant attention. ST devices have been intensively developed and investigated: CDX-U[15,16], MAST[17], NSTX[18,19], PEGASUS[20,21], LATE[22], TST-2[23], SUNIST[24] and QUEST[25–28].

Although removing TF coils from tokamak is impossible, if we can substitute Ohmic initiation in another way, compact ST reactor may be feasible. Substitution of Ohmic initiation means elimination of CS from the inward of torus. Without CS, an alternative method to start plasma should be developed. In ST research, in addition to the investigation toward understanding high-β plasma, non-inductive initiation and current drive are the key issues.

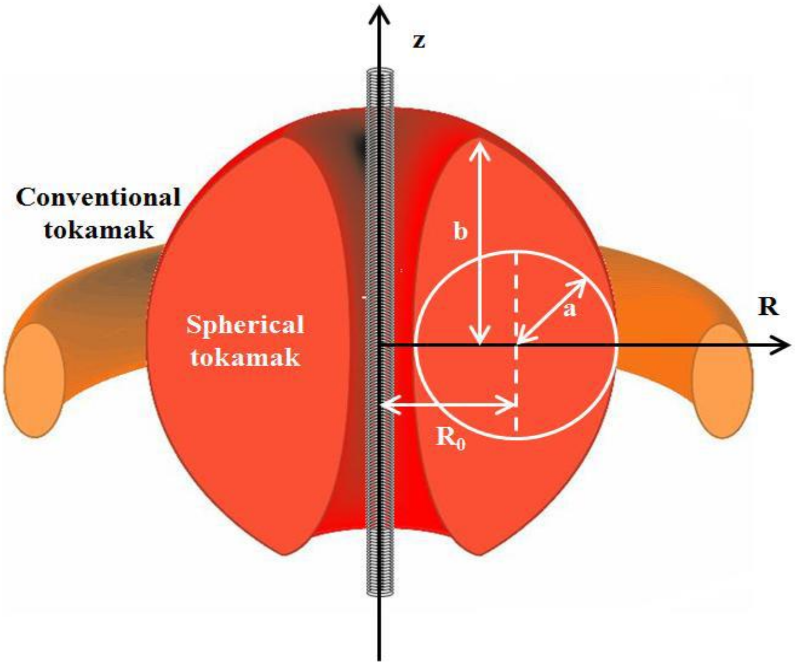

Fig. 1-4. Comparison of conventional tokamak and spherical tokamak configurations

1.4 Conceptual Design of Tokamak Reactor

We have discussed on tokamak type of plasma magnetic confinement of plasma. Besides, there is a wide range of design approaches: tokamak, stellarator, spherical tokamak (ST), reversed-field pinch (RFP), spheromak, field-reversed configuration (FRC) and tandem mirror (TM). Since 1960s to present, 50 conceptual power plant design studies have been conducted worldwide[29]. In Ref. 29, detailed explanations are denoted. We do not focus to investigate the differences of those types of magnetic confinement. Therefore, in Fig. 10, the timeline of conceptual power plant designs is presented. Tokamak type has been frequently developed as a whole. However, after 1980, it had started designing other types of reactor for 10 years and then shifted to tokamak again. This process shows that tokamak type has been elected as the most promising for fusion reactor. When we look into recent concepts of reactor, we can find a trend that compactness has become important. Slim CS designed in Japan employs ST configuration for economical[30]. Compactness can directly contribute to the cost-effectiveness since larger device gives rise of construction cost[31].

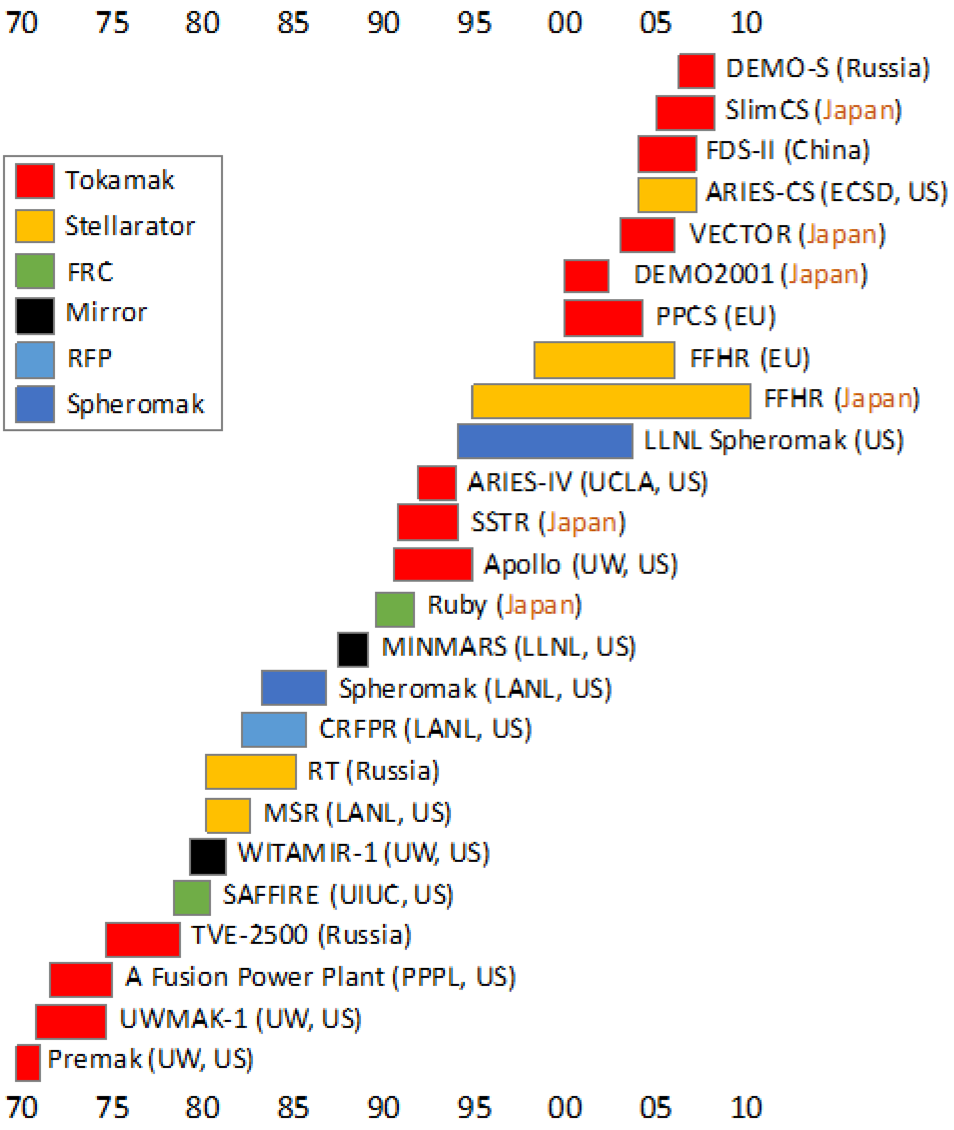

Fig. 1-4. Timeline of large-scale conceptual power plant designs developed worldwide for magnetic fusion.

1.5 Thesis Objective

Development of ST-based fusion reactor has a striking influence in the viewpoint of cost-effectiveness. Since STs do not have an enough space for CS, auxiliary heating methods are required to initiate plasma (breakdown and current drive). NBI is only for the phase where adequate plasma density developed for momentum transfer so that RF wave injection is preferable in the breakdown phase. Moreover, in ITER plan[4,32,33], they are going to employ RF injection in the range of electron cyclotron (EC) to support the inductive breakdown by CS. Intensive studies had promoted in many devices to obtain a reliable breakdown with electron cyclotron resonance heating (ECRH). Consequently, there remain no technical problems to realize a reliable breakdown in ITER with ECRH-assist and its plan has not been changed for more than 10 years. However, compared with inductive breakdown, systematic investigation has not been done for RF-induced breakdown itself. Experiments with ECRH tend to focus on plasma current after breakdown[34]. Understanding RF-induced breakdown has a possibility to improve the conventional inductive breakdown with RF-assist method. Conditions for RF-induced breakdown cannot be illustrated in the same way with inductive one since the direction of acceleration of electrons is different. In this Ph.D. thesis, by applying the electron loss scheme onto RF-breakdown, therefore, the conditions and optimization of RF-induced breakdown will be presented.

The structure of this Ph.D. thesis is as following. In Chapter 2, wave propagation in plasma and energy transfer mechanism by ECRH are described. In Chapter 3, detailed RF-induced review is provided. Next, in Chapter 4, experimental set-up and equipment of the QUEST spherical tokamak are specified. In Chapter 5, model development to illustrate breakdown phase is denoted. In Chapter 6, we present experimental results and modeling analysis to investigate RF-breakdown conditions. Finally in Chapter 7, given a conclusion and future works are designed.

Refs in Chapter 1

[1] J. Wesson, *Tokamaks Third Edition* (2004).

[2] G.L. Jackson, P.A. Politzer, D.A. Humphreys, T.A. Casper, A.W. Hyatt, J.A. Leuer, J. Lohr, T.C. Luce, M.A. Van Zeeland, and J.H. Yu, Phys. Plasmas **17**, (2010).

[3] D.C. Pace, W.W. Heidbrink, and M.A. Van Zeeland, Phys. Today **68**, 34 (2015).

[4] ITER Physics Expert Groups, Nucl. Fusion **39**, 2577 (1999).

[5] H.P. Furth, Nucl. Fusion **15**, 487 (1975).

[6] N.J. PEACOCK, D.C. ROBINSON, M.J. FORREST, P.D. WILCOCK, and V. V SANNIKOV, Nature **224**, 488 (1969).

[7] K.U. and Y.G. and T.Y. and N.S. and M.M. and T.H. and M.S. and S.K. and N. Fujisawa, Plasma Phys. **21**, 89 (1979).

[8] K. Molvig, S.P. Hirshman, and J.C. Whitson, Phys. Rev. Lett. **43**, 582 (1979).

[9] G.M. McCracken, S.J. Fielding, S.K. Erents, A. Pospieszczyk, and P.E. Stott, Nucl. Fusion **18**, 35 (1978).

[10] F. Wagner, G. Becker, K. Behringer, D. Campbell, A. Eberhagen, W. Engelhardt, G. Fussmann, O. Gehre, J. Gernhardt, and G. v Gierke, Phys. Rev. Lett. **49**, 1408 (1982).

[11] D. Van Houtte and E.T. Supra, Nucl. Fusion **33**, 137 (1993).

[12] J.E.T. Team, Nucl. Fusion **32**, 187 (1992).

[13] K.M. McGuire, H. Adler, P. Alling, C. Ancher, H. Anderson, J.L. Anderson, J.W. Anderson, V. Arunasalam, G. Ascione, and D. Ashcroft, Phys. Plasmas **2**, 2176 (1995).

[14] S. Ishida, T. Fujita, H. Akasaka, N. Akino, K. Annou, T. Aoyagi, T. Arai, K. Arakawa, N. Asakura, and M. Azumi, Phys. Rev. Lett. **79**, 3917 (1997).

[15] C.B. Forest, Y.S. Hwang, M. Ono, G. Greene, T. Jones, W. Choe, M. Schaffer, A. Hyatt, T. Osborne, and R.I. Pinsker, Phys. Plasmas **1**, 1568 (1994).

[16] C.B. Forest, Y.S. Hwang, M. Ono, and D.S. Darrow, Phys. Rev. Lett. **68**, 3559 (1992).

[17] V.F. Shevchenko, M.R. O'Brien, D. Taylor, and A. N. Saveliev, Nucl. Fusion **50**, 22004 (2010).

[18] M. Ali Asgarian, A. Parvazian, M. Abbasi, and J.P. Verboncoeur, Phys. Plasmas **21**, (2014).

[19] F. Ebrahimi and R. Raman, Phys. Rev. Lett. **114**, 1 (2015).

[20] D.J. Battaglia, M.W. Bongard, R.J. Fonck, and A.J. Redd, Nucl. Fusion **51**, 73029 (2011).

[21] J.B. O'Bryan, C.R. Sovinec, and T.M. Bird, Phys. Plasmas **19**, 80701 (2012).

[22] H. Tanaka, M. Uchida, T. Yoshinaga, J. Yamada, S. Yamaguchi, and T. Maekawa, AIP Conf. Proc. **787**, 415 (2005).

[23] T. Shinya, Y. Takase, T. Wakatsuki, A. Ejiri, H. Furui, J. Hiratsuka, K. Imamura, T. Inada, H. Kakuda, H. Kasahara, R. Kumazawa, C. Moeller, T. Mutoh, Y. Nagashima, K. Nakamura, A. Nakanishi, T. Oosako, K. Saito, T. Seki, M. Sonehara, H. Togashi, S. Tsuda, N. Tsujii, and T. Yamaguchi, Nucl. Fusion **55**, 73003 (2015).

[24] H. Ye-xi, Plasma Sci. Technol. **4**, 1355 (2002).

[25] K. Hanada, H. Zushi, H. Idei, K. Nakamura, M. Ishiguro, S. Tashima, E.I. Kalinikova, M. Sakamoto, M. Hasegawa, A. Fujisawa, A. Higashijima, S. Kawasaki, H. Nakashima, H. Liu, O. Mitarai, T. Maekawa, A. Fukuyama, Y. Takase, and J. Qian, Plasma Sci. Technol. **13**, (2011).

[26] M. Ishiguro, K. Hanada, H. Liu, R. Ogata, M. Isobe, S. Tashima, H. Zushi, K. Sato, A. Fujisawa, K. Nakamura, H. Idei, M. Sakamoto, M. Hasegawa, Y. Takase, T. Maekawa, Y. Kishimoto, O. Mitarai, S. Kawasaki, H. Nakashima, and A. Higashijima, J. Phys. Conf. Ser. **511**, 12041 (2014).

[27] S. Tashima, H. Zushi, M. Isobe, K. Hanada, H. Idei, K. Nakamura, a. Fujisawa, K. Matsuoka, M. Hasegawa, Y. Nagashima, S. Okamura, S. Banerjee, S. Kawasaki, H. Nakashima, and a. Higashijima, Nucl. Fusion **54**, 23010 (2014).

[28] R. Yoneda, K. Hanada, K. Nakamura, H. Idei, N. Yoshida, M. Hasegawa, T. Onchi, K. Kuroda, S. Kawasaki, A. Higashijima, T. Nagata, A. Isayama, O. Mitarai, A. Fukuyama, and Y. Takase, Cit. Phys. Plasmas **24**, (2017).

[29] L.A. El-Guebaly, Energies **3**, 1067 (2010).

[30] S. Nishio, K. Tobita, S. Konishi, T. Ando, S. Hiroki, T. Kuroda, M. Yamauchi, M. Azumi, and M. Nagata, 19th IAEA Intl. Conf. Fusion Energy. 1 (2002).

[31] R. Yoneda, Evergr. Jt. J. Nov. Carbon Resour. Sci. Green Asia Strateg. **4**, 16 (2017).

[32] B. Lloyd, P.G. Carolan, and C.D. Warrick, Plasma Phys. Control. Fusion **38**, 1627 (1996).

[33] J. Stober, G.L. Jackson, E. Ascasibar, Y.-S. Bae, J. Bucalossi, A. Cappa, T. Casper, M.-H. Cho, Y. Gribov, G. Granucci, K. Hanada, J. Hobirk, A.W. Hyatt, S. Ide, J.-H. Jeong, M. Joung, T. Luce, T. Lunt, W. Namkung, S.-I. Park, P. a. Politzer, J. Schweinzer, and A.C.C. Sips, Nucl. Fusion **51**, 83031 (2011).

[34] C.B. Forest, Y.S. Hwang, M. Ono, G. Greene, T. Jones, W. Choe, M. Schaffer, A. Hyatt, T. Osborne, R.I. Pinsker, C.C. Petty, L. J, and S. Lippmann, Phys. Plasmas **1**, 1568 (1994).

2. Electron Cyclotron Resonance Heating of Plasma

Electrons immersed in magnetic fields gyrate due to Lorentz force along with magnetic line of force. This gyration is called cyclotron motion and by injecting electromagnetic waves at integer multiple of the cyclotron frequency, resonance between wave and plasma enables energy transfer. Electron Cyclotron Resonance Heating (ECRH)[1–7] employs this mechanism of energy transfer to heat plasma up to higher temperature. Namely, ECRH heats up electrons but if energy confinement time of a device is longer than that of temperature relaxation between ions and electrons, ions can be eventually heated up.

Let us start with a charged particle only in static magnetic induction $\boldsymbol{B}$. The particle with charge q, mass m and moving velocity $\boldsymbol{v}$ feels Lorentz force and the equation of motion is,

$$m\frac{d\boldsymbol{v}}{dt} = q(\boldsymbol{v} \times \boldsymbol{B}). \qquad 2.1$$

At our convenience, we shall divide $\boldsymbol{v}$ in two components: parallel $\boldsymbol{v}_\parallel$ and perpendicular $\boldsymbol{v}_\perp$ to the magnetic field $\boldsymbol{B}$. Nothing that the parallel component of (2.1) vanishes and leaving only the perpendicular component as,

$$\frac{d\boldsymbol{v}_\perp}{dt} = \frac{q}{m}(\boldsymbol{v}_\perp \times \boldsymbol{B}), \qquad 2.2$$

By introducing $\boldsymbol{\Omega}_c$, we can rewrite the equation as,

$$\frac{d\boldsymbol{v}_\perp}{dt} = \boldsymbol{\Omega}_c \times \boldsymbol{v}_\perp, \qquad 2.3$$

where $\boldsymbol{\Omega}_c$ is a vector defined by,

$$\boldsymbol{\Omega}_c = -\frac{q\boldsymbol{B}}{m} = \frac{|q|\boldsymbol{B}}{m}\widehat{\boldsymbol{\Omega}}_c = \Omega_c\widehat{\boldsymbol{\Omega}}_c. \qquad 2.4$$

Here, we integrate (2.3) in time and taking $\boldsymbol{v}_\perp = d\boldsymbol{r}_c/dt$,

$$\boldsymbol{v}_\perp = \boldsymbol{\Omega}_c \times \boldsymbol{r}_c, \qquad 2.5$$

where $\boldsymbol{r}_c$ is the positon of particle with respect to the guiding center in the plane perpendicular to $\boldsymbol{B}$. Then, $\boldsymbol{\Omega}_c$ is the angular velocity and the magnitude Ω_c is known as cyclotron frequency. For electron cyclotron frequency Ω_{ce}, with $|q| = 1.602 \times 10^{-19}$ [C] and $m = 9.109 \times 10^{-19}$ [kg],

$$\Omega_{\mathrm{ce}} = 1.76 \times 10^{11} B \ \ [\mathrm{rad/s}], \qquad 2.6$$

with B in tesla. Equivalently in Hz, $f_{\mathrm{ce}} \sim 28B$ [GHz]. Important fact here is that cyclotron frequency is directly proportional to magnetic field magnitude $\boldsymbol{B}$. Locations of ECR layer where interaction of EC wave and electrons occurs can be decided by a magnetic profile of a device and an injected RF frequency. Both magnetic field and RF frequency depends on experimental equipment. Torus fusion devices such as tokamak and helical systems, magnetic field (toroidal field) decays proportionally to the radial direction of the torus. As for RF frequency, high-power oscillators (Klystron, Gyrotron and Magnetron) can usually operate at one fixed frequency. RF wave must pass through vacuum and plasma to reach for the ECR layer. Except around the ECR layer, cold plasma approximation describes well the wave propagation inside plasma. Hereby, around the ECR layer, wave phase velocity is equivalent or less compared to thermal velocity of plasma particles (electrons). Therefore, an interaction of wave and thermal motions cannot be neglected and that is when energy transfer happens. We will discuss the mechanism of energy transfer later but in the next section we first denote the wave propagation inside plasma with cold approximation. The explanation and discussion are based on references[8,9].

2.1 Waves in Cold Plasma

Cold theory provides rich information of wave propagation in plasma and is a very powerful tool for plasma analysis and diagnostics. In the cold model, the thermal kinetic energy of plasma (ions and electrons) is ignored and corresponding velocity distribution employs a Dirac delta function centered at the macroscopic fluid velocity. To derive the cold dispersion relationship, we start with two Maxwell equations;

$$\nabla \times \boldsymbol{E} = -\frac{\partial \boldsymbol{B}}{\partial t}, \qquad 2.7$$

$$\nabla \times \boldsymbol{B} = \mu_0 (\boldsymbol{J} + \varepsilon_0 \frac{\partial \boldsymbol{E}}{\partial t}) = \frac{1}{c^2} \frac{\partial \boldsymbol{D}}{\partial t}, \qquad 2.8$$

where, $\boldsymbol{E}$ is the electric field, $\boldsymbol{J}$ is the current density, μ_0 is the vacuum permeability and ε_0 is the vacuum dielectric constant. $\boldsymbol{D}$ is electric displacement and with Fourier analysis in space and time,

$$\boldsymbol{D}(\omega, \boldsymbol{k}) = \boldsymbol{\epsilon}(\omega, \boldsymbol{k}) \cdot \boldsymbol{E}(\omega, \boldsymbol{k}) = \frac{i}{\omega \varepsilon_0} \boldsymbol{J}(\omega, \boldsymbol{k}) + \boldsymbol{E}(\omega, \boldsymbol{k}), \qquad 2.9$$

where $\boldsymbol{\epsilon}$ is the dielectric tensor. The plasma current is expressed in terms of the macroscopic particle velocities,

$$\boldsymbol{J} = \sum_s \boldsymbol{j}_s = \sum_s n_s q_s \boldsymbol{v}_s, \qquad 2.10$$

where n_s is the number density of particles of species *s* with charge q_s. In the cold model, we ignore the ion motion that $q_s = -e$. Consequently, $\boldsymbol{J} = -en_e\boldsymbol{v}_e$. The two equations (2.7) and (2.8) can be combined to show the equation of wave propagation,

$$\boldsymbol{k} \times (\boldsymbol{k} \times \boldsymbol{E}) + \frac{\omega^2}{c^2} \boldsymbol{\epsilon} \cdot \boldsymbol{E} = 0, \qquad 2.11$$

Electrons in the cold model follow the Langevin equation of motion,

$$m \frac{D\boldsymbol{v}_e}{Dt} = q(\boldsymbol{E} + \boldsymbol{v}_e \times \boldsymbol{B}) - m\nu \boldsymbol{v}_e, \qquad 2.12$$

the second term of right hand side is the moment transfer rate with collision frequency ν. For simplicity, we consider only the first-order terms of (2.12) and collision-less plasma. Then, after Fourier analysis,

$$-i\omega m \boldsymbol{v}_e = q(\boldsymbol{E} + \boldsymbol{v}_e \times \boldsymbol{B}_0), \qquad 2.13$$

where $\boldsymbol{B}_0$ is a constant field, static in time and uniform in space. That is, $\boldsymbol{B} = \boldsymbol{B}_0 + \boldsymbol{B}_1(\boldsymbol{r}, t)$. We set the direction of $\boldsymbol{B}_0$ as $\boldsymbol{B}_0 = B_0\hat{\boldsymbol{z}}$ in a Cartesian coordinate (x, y, z). Using (2.9), (2.10), (2.11) and (2.13), we obtain the dielectric tensor,

$$\boldsymbol{\epsilon} = \begin{bmatrix} S & -iD & 0 \\ -iD & S & 0 \\ 0 & 0 & P \end{bmatrix}, \tag{2.14}$$

where $\mathrm{S, D, P}$ is Stix parameters[9] defined by

$$S = \frac{1}{2}(R + L), \tag{2.15}$$

$$D = \frac{1}{2}(R - L), \tag{2.16}$$

$$R = 1 - \frac{\Omega_{\mathrm{pe}}^2}{\omega(\omega + \Omega_{\mathrm{ce}})}, \tag{2.17}$$

$$L = 1 - \frac{\Omega_{\mathrm{pe}}^2}{\omega(\omega - \Omega_{\mathrm{ce}})}, \tag{2.18}$$

$$P = 1 - \frac{\Omega_{\mathrm{pe}}^2}{\omega^2}. \tag{2.19}$$

Ω_{pe} is the plasma frequency expressed as $\Omega_{\mathrm{pe}} = \sqrt{\frac{n_{\mathrm{e}} e^2}{m_{\mathrm{e}} \varepsilon_0}}$. Now we have the expression of the dielectric tensor $\boldsymbol{\epsilon}$. Next is to solve the wave equation (2.11). It is convenient to introduce the refractive index, which is dimensionless;

$$\boldsymbol{n} = \frac{\boldsymbol{k}c}{\omega}. \tag{2.20}$$

The wave equation (2.11) simply becomes,

$$\boldsymbol{n} \times (\boldsymbol{n} \times \boldsymbol{E}) + \boldsymbol{\epsilon} \cdot \boldsymbol{E} = 0. \tag{2.21}$$

The wave number vector is set to $\boldsymbol{k} = k\sin\theta\hat{\boldsymbol{x}} + k\cos\theta\hat{\boldsymbol{z}}$, then, $\boldsymbol{n}$ is also in the plane x-z plane. Eq. (2.14) turns into,

$$\begin{pmatrix} S - n^2\cos^2\theta & -iD & n^2\cos\theta\sin\theta \\ iD & S - n^2 & 0 \\ n^2\cos\theta\sin\theta & 0 & P - n^2\sin^2\theta \end{pmatrix} \begin{pmatrix} E_{\mathrm{x}} \\ E_{\mathrm{y}} \\ E_{\mathrm{z}} \end{pmatrix} = 0. \tag{2.22}$$

The determinant of the wave equation (2.22) must vanish. The condition is called *dispersion relation* that gives oscillation modes of the system considered. The cold dispersion relation (2.22) is also possible to write in a different way, which is Appleton-Hartree equation,

$$An^4 - Bn^2 + C = 0, \tag{2.23}$$

$$A = S\sin^2\theta + P\cos^2\theta, \tag{2.24}$$

$$B = RL\sin^2\theta + PS(1 + \cos^2\theta), \tag{2.25}$$

$$C = PRL. \tag{2.26}$$

Solving (2.23) and manipulating to find

$$n^2 = 1 - \frac{2(A - B + C)}{2A - B \pm \sqrt{B^2 - 4AC}}, \tag{2.27}$$

These procedures are the same with solving (2.22) and analytically useful. If we set refractive index like this, it is just matter of mathematics. For examples, the dispersion relation goes for the propagation parallel ($\theta = 0$) and perpendicular ($\theta = \pi/2$) to the magnetic field,

$$P = 0, n^2 = R, n^2 = L \ \ (\theta = 0), \tag{2.28}$$

$$n^2 = P, n^2 = \frac{RL}{S} \ \ (\theta = \pi/2). \tag{2.29}$$

In this thesis, we discuss mainly the perpendicular propagation to the static magnetic field (toroidal field). The dispersion relation (2.29) shows that there exist two wave modes of propagation. First is ordinary mode usually referred as O-mode,

$$\begin{aligned} n_{\mathrm{O}}^2 &= P \\ &= 1 - \frac{\omega_{\mathrm{pe}}^2}{\omega^2} \end{aligned} \tag{2.30}$$

As it is, the O-mode dispersion does not contain the term of magnetic field but only electron density. That is, it is not affected by the magnetic field when it travels. The other mode is called extraordinary mode (X-mode),

$$n_{\mathrm{X}}^2 = \frac{RL}{S} = \frac{(\omega^2 - \omega_{01}^2)(\omega^2 - \omega_{02}^2)}{\omega^2(\omega^2 - \omega_{\mathrm{uh}}^2)}, \tag{2.31}$$

where ω_{01} and ω_{02} are defined by,

$$\omega_{01} = \frac{1}{2}\left[-\Omega_{\mathrm{ce}} + \left(\Omega_{\mathrm{ce}}^2 + 4\omega_{\mathrm{pe}}^2\right)^{\frac{1}{2}}\right], \tag{2.32}$$

$$\omega_{02} = \omega_{01} + \Omega_{\mathrm{ce}}. \tag{2.33}$$

ω_{uh} is the upper hybrid resonance (UHR) frequency,

$$\omega_{\mathrm{uh}} = (\omega_{\mathrm{pe}}^2 + \Omega_{\mathrm{ce}}^2)^{\frac{1}{2}}. \tag{2.34}$$

O-mode only has a reflection point (cutoff) when $P = 0$. X-mode has two reflection points when $R = 0$ or $L = 0$ and also has a resonance point at ω_{uh}. Figure 2-1 is the CMA diagram, showing resonance and reflection conditions. Two examples of wave propagation are shown ($\omega_{\mathrm{pe}} < \Omega_{\mathrm{ce}}$): low field side (LFS) O-mode and HFS X-mode. O-mode do not sees R cutoff and UHR so it only does the plasma cutoff. Before the over-dense, O-mode can reach to the fundamental ECR. Next, X-mode from HFS first pass through the fundamental ECR with little absorption ($\theta = \pi/2$) and hit the UHR layer. Then X-mode can be converted into an electron static wave so-called electron Bernstein wave (EBW). EBW is fully damped near the cyclotron harmonics.

In QUEST experiments until 2017, all launchers for ECRH have been located at LFS. In Chapter 4 of experiment apparatus, detailed information of RF launcher is presented.

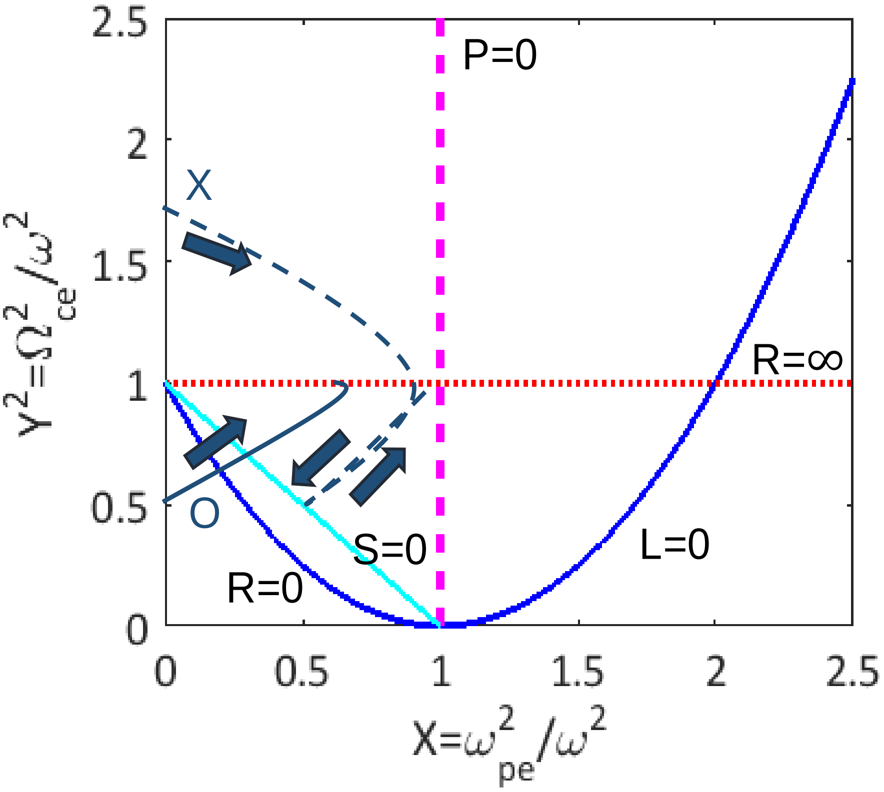

Fig. 2-1. CMA diagram. Red dot line is the 1st ECR layer. Pink dash line is O-mode (plasma) cutoff. Blue line is X-mode cutoff corresponds to R and L cutoffs. Light blue line is the upper hybrid resonance. O and X-mode projection are presented when $\omega_{pe} < \Omega_{ce}$ is satisfied. The area in-between S=0 and R=0 is the evanescent layer that X-mode cannot propagate.

2.2 Cyclotron Wave Damping

So far in this chapter, wave propagation perpendicular to the static magnetic field $\boldsymbol{B}_0$ with cold model has been given. Now, we start to consider how traveling wave interacts with electrons at the cyclotron resonance. To keep generality of low field side RF injection in tokamak configuration, we first assume that O-mode or X-mode are propagating approximately perpendicular to $\boldsymbol{B}_0$.
The cyclotron resonance condition neglecting the relativistic effect is nothing that,

$$\omega - n\Omega_{\mathrm{ce}} - k_{\parallel}v_{\parallel} = 0, \qquad 2.35$$

where n is the harmonic number and the third term is Doppler shift effect. As for X-mode, which has an electric field component on the plane perpendicular to $\boldsymbol{B}_0$, the physical picture of cyclotron damping is easy to illustrate that electrons gyrating along $\boldsymbol{B}_0$ can interact with wave and wave loses its energy.

On the other hand, for O-mode, which only have an electric field component on the plane parallel to $\boldsymbol{B}_0$, we need another treatment. The average force $\langle F_{\parallel}\rangle$ that electrons feel by $\boldsymbol{E}_{\parallel}$ of O-mode is expressed as[10,11],

$$\langle F_{\parallel}\rangle = -\sum_{n=-\infty}^{\infty} \frac{eE_{\parallel}\omega}{2\pi}\int_0^{\frac{2\pi}{\omega}} dt\, J_n(k_{\perp}\rho_e)\exp(-i(\omega - n\Omega_{\mathrm{ce}} - k_{\parallel}v_{\parallel})t + in\varphi), \qquad 2.36$$

where ρ_e is Larmor radius of electron and J_n is the modified Bessel function. When the resonance condition is satisfied, electrons feel constant force in the parallel direction and energy transfer between wave and electrons occurs. Important note here is that since the expression includes ρ_e, the thermal electron effect is necessary for energy transfer. To quantitatively investigate cyclotron damping at the fundamental ECR layer for X-mode and O-mode propagating nearly perpendicular to $\boldsymbol{B}_0$, the optical thickness for both modes are described as,

$$\Gamma(\mathrm{X}) = \frac{\pi^2}{2}\beta_e^2\cos^2\theta\,\frac{\{2+q(1-q)\}^2(2-q)^{\frac{1}{2}}}{q}\frac{R_0}{\lambda_0}, \qquad 2.37$$

$$\mathit{\Gamma}(0) = \frac{\pi^2}{2}\beta_e^2 q(1-q)^{\frac{1}{2}}\frac{R_0}{\lambda_0}, \qquad 2.38$$

where R_0 is the major radius of torus, $\lambda_0 = 2\pi/k_0$ is the free space wavelength, $\beta_e = v_{te}/c$ is the ratio of electron thermal velocity v_{te} to the light speed and q is defined as $q = (\omega_{pe}/\Omega_{\mathrm{ce}})^2$. If $\mathit{\Gamma}(\mathrm{X}, 0) > 1$, RF wave can be completely absorbed to the plasma when crossing the torus. The optical thickness discussed above only valid when we include the effect of electron thermal velocity $(q \gg \beta_e)$.

In summary of Chapter 2, wave propagation in the range of EC with cold model and absorption by cyclotron damping with electron thermal velocity are specified. All derivations and specifications assume the presence of plasma particles so that the plasma breakdown, which is the main theme of this Ph.D. thesis, another description in breakdown phase is required and will be specified in the next chapter.

Refs in Chapter 2

[1] V. Erckmann and U. Gasparino, Plasma Phys. Control. Fusion **36**, 1869 (1994).

[2] R. Prater, R.J. Buttery, J. DeBoo, J.R. Ferron, A. Garofalo, C.T. Holcomb, G.L. Jackson, R.J. La Haye, J.M. Lohr, T.C. Luce, C.C. Petty, P.A. Politzer, W.M. Solomon, and F. Turco, EPJ Web Conf. **32**, 2010 (2012).

[3] B. Lloyd, G.L. Jackson, T.S. Taylor, E. a. Lazarus, T.C. Luce, and R. Prater, Nucl. Fusion **31**, 2031 (1991).

[4] J. Stober, G.L. Jackson, E. Ascasibar, Y.-S. Bae, J. Bucalossi, A. Cappa, T. Casper, M.-H. Cho, Y. Gribov, G. Granucci, K. Hanada, J. Hobirk, A.W. Hyatt, S. Ide, J.-H. Jeong, M. Joung, T. Luce, T. Lunt, W. Namkung, S.-I. Park, P. A. Politzer, J. Schweinzer, and A.C.C. Sips, Nucl. Fusion **51**, 83031 (2011).

[5] G.L. Jackson, D. A. Humphreys, A. W. Hyatt, J.M. Lohr, T.C. Luce, and J.H. Yu, Nucl. Fusion **51**, 83015 (2011).

[6] G.L. Jackson, J.S. Degrassie, C.P. Moeller, and R. Prater, Nucl. Fusion **47**, 257 (2007).

[7] B. Lloyd, Plasma Phys. Control. Fusion **40**, A119 (1998).

[8] J.A. Bittencourt, *Fundamentals of Plasma Physics* (Springer Science & Business Media, 2013).

[9] T.H. Stix, *Waves in Plasmas* (Springer Science & Business Media, 1992).

[10] S. Takamura, *Plasma Heating Theory (in Japanese)* (1986).

[11] A.G. Litvak, G. V. Permitin, E. V. Suvorov, and A.A. Frajman, Nucl. Fusion **17**, 659 (1977).

3. Review of RF-induced Breakdown of Plasma

This chapter gives a review of RF-induced breakdown of tokamak plasma. Physical illustration and experimental evidence with different tokamaks will be presented.

Breakdown is the first step of plasma build-up and so that we would like to begin with a conventional understanding of plasma breakdown. When an electric field is applied to partially ionized gas, electrons and ions are being accelerated to respective directions and collide with gas molecules, and then produces new electrons and ions[1,2]. In Fig. 3-1, a gas inserted between electrodes with infinite distance d. When we apply a voltage V to the circuit, electrons can be released from the cathode. After a number of collisions, a primary electron reaches to equilibrium energy and produces α electrons and α positive ions on its way between the electrodes. α is usually referred as Townsend first coefficient. It is well-known that α depends on the constant field $X = V/d$, pressure p and gas species. The number of electrons is simply expressed by integrating from cathode to anode,

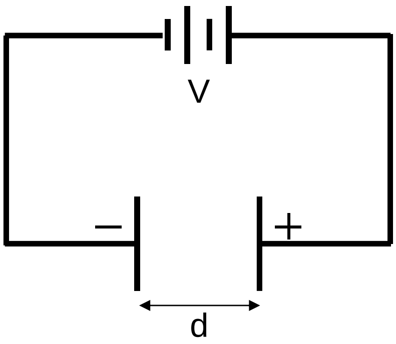

Fig. 3-1. Schematic of gas discharge interposed by two

$$N = N_0 \exp(\alpha d) \tag{3.1}$$

where N_0 is the initial number of electrons at cathode. Another important factor to be included in that the secondary effects that ions hitting the cathode liberate secondary electrons,

$$N = N_0 \frac{\exp(\alpha d)}{1 - \gamma(\exp(\alpha d) - 1)} \tag{3.2}$$

where γ is the number of electrons produced by one ion arriving the cathode, and is referred as Townsend second coefficient. Form the Eq. 3.2, we can get the condition for ‘breakdown’ in-between the electrodes,

$$\gamma(\exp(\alpha d) - 1) = 1 \qquad 3.3$$

This condition states that the initial seed discharge can enter into a self-sustainable discharge. Under the condition, there requires no N_0 at the cathode. To use Eq. 3.3 for modeling breakdown phase, we further need to specify the relation of α and X. Based on semi-empirical knowledge, that is,

$$\alpha/p = A\exp(-B/(X/p)) \qquad 3.4$$

where $A = 1/\lambda_1, B = V_i/\lambda_1,$ and λ_1 is a mean free path λ at $p = 1$ due to standardization. In practical, for hydrogen we use in fusion experiments, $A = 3.83\ [\mathrm{m}^{-1} \cdot \mathrm{Pa}^{-1}]$ and $B = 1.04 \times 10^2\ [\mathrm{V} \cdot \mathrm{m}^{-1} \cdot \mathrm{Pa}^{-1}]$ are valid in broad range.

3.1 Ohmic Breakdown in ITER

We see that breakdown of plasma in-between electrodes provides a conventional illustration of self-sustainable discharge. Stretching this mechanism toward tokamak magnetic configuration, we discuss on 'Ohmic (Inductive) breakdown' in ITER, for instance. Since many physics and technical difficulties are to be demonstrated in ITER, it gives beneficial aspects that discussion on ITER is equivalently to speak of general interests in tokamak devices.

Matter of course, the plasma initiation in ITER employs Ohmic breakdown[3–5] and has been a critical issue since technical difficulties of vessel thickness and superconducting coils set a limitation that the loop voltage of center solenoid must be less than 0.3 V/m. In previous section, we assumed that there was no loss mechanism such as lateral diffusion between electrodes. However, in the presence of magnetic field in tokamak configuration, loss schemes such as drift loss across magnetic field cannot be negligible[6]. We shall start with the representation of production and disappearance of electrons as,

$$\frac{dn_\mathrm{e}}{dt} = n_\mathrm{e}\left(\tau_\mathrm{ion}^{-1} - \tau_\mathrm{loss}^{-1}\right) \qquad 3.5$$

where τ_ion and τ_loss are the ionization and loss rate, respectively. Now we deal with expression in time, that is, a discussion on avalanche of electrons is attainable. In the electron avalanche in tokamak, there are two main loss schemes: drift loss and direct loss along magnetic field. First, the drift loss can be caused by curvature and $\nabla\boldsymbol{B}$ drift across the magnetic field. The drift velocity of guiding center is expressed by,

$$v_{\mathrm{drift}} = \frac{1}{R\Omega_{\mathrm{ce}}}\left(\frac{1}{2}v_{\perp}^2 + v_{\parallel}^2\right) \qquad 3.6$$

where R is the major radius of the torus, $v_{\perp}$ and $v_{\parallel}$ are the velocity perpendicular and parallel to the magnetic line of force, respectively. An important note that a larger toroidal field gives a suppression of the drift loss, enhancing Ω_{ce}. In case of dominant drift loss, τ_{loss} goes,

$$\tau_{\mathrm{loss}} = \frac{a}{v_{\mathrm{drift}}}, \qquad 3.7$$

where a is the minor radius of the torus. Secondly, the direct loss comes from an inability to make a perfect torus symmetry field due to an error field of coils. Because of the error field, a trace of magnetic line of force must touch the vessel walls, which is the disappearance of plasma particles. For the expression of direct loss velocity v_{direct}, if we assume that an electron gains constant energy after a few collisions,

$$v_{\mathrm{direct}} = \eta X/p \qquad 3.8$$

The value of coefficient η should be taken to approximately 43 before the entrance to runaway regime. That is, this assumption is reasonable in the beginning of Ohmic breakdown phase. When the direct loss is superior,

$$\tau_{\mathrm{loss}} = \frac{L}{v_{\mathrm{direct}}} = \frac{a\,B_t/B_{\perp}}{v_{\mathrm{direct}}}, \qquad 3.9$$

where L is the connection length (a trace of magnetic line of force), B_{t} is the toroidal field and $B_{\perp}$ is the error field in the direction perpendicular to L. On the discussion by B. Lloyd *et al.*[6], we can assume that the direct loss is superior in usual case from viewpoint of experiments. Therefore, the condition of Ohmic breakdown is when L is at least larger than ionization length α^{-1}. Finally, we derive the requirement for Ohmic breakdown for hydrogen,

$$E_{\min} = \frac{1.39 \times 10^4 p[\mathrm{Torr}]}{\ln(510 \cdot p[\mathrm{Torr}] \cdot L[\mathrm{m}])}, \qquad 3.10$$

where $E_{\min}$ is the minimum electric field required for Ohmic breakdown. Figure 3-2 illustrates the relation of $E_{\min}$ and p with different values of L. At convenience, the dimension of p is in [Pa] in Fig. 3-2.

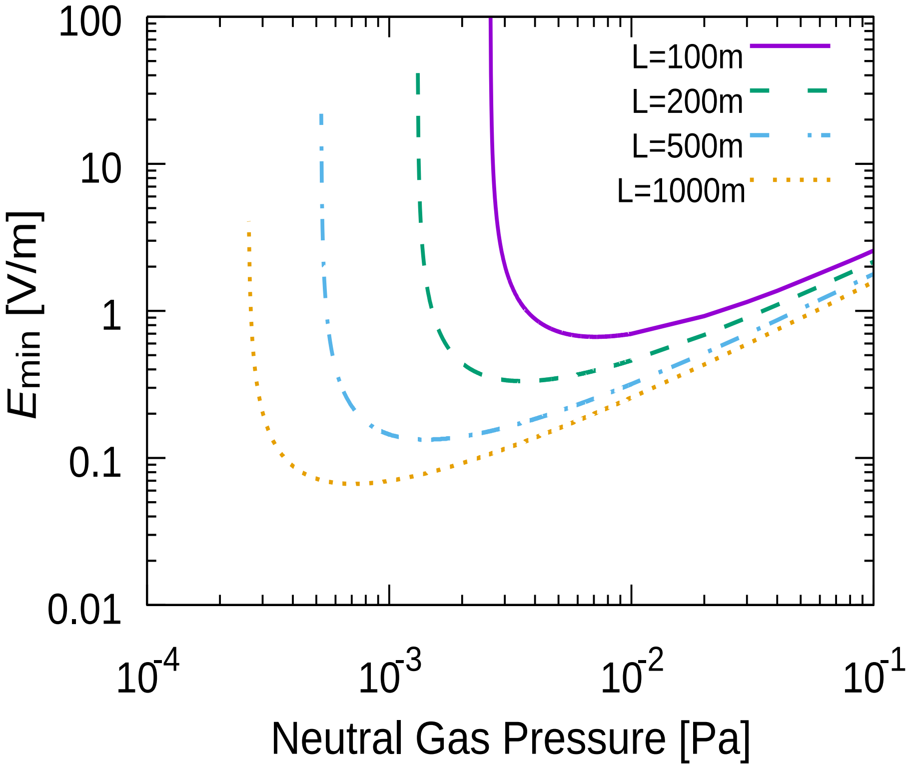

Fig. 3-2. The relation of minimum electric field requirement and neutral gas pressure (hydrogen) with different connection length of magnetic lines of force for inductive breakdown of plasma.

The operational range in smaller $E_{\min}$ is very narrow but making connection length longer broadens the range. For ITER, there have been research activities to ensure the feasibility of plasma breakdown. In Fig. 3-3, it shows a comparison with experiments. Experimental results with Ohmic and RF-assisted breakdown are specified in DIII-D and JT-60U tokamaks. In JT-60U, usual Ohmic breakdown takes place with 0.8 V/m, which is well above the requirement for ITER. RF-assisted Ohmic breakdown gives a significant reduction of $E_{\min}$ both for lower hybrid (LH) and EC heating. In DIII-D with EC injection (700kW, 60GHz), $E_{\min}$ of 0.25 V/m was attainable with deuterium ($\mathrm{D_2}$). In JT-60U, LH assistance realized a huge reduction that a breakdown at 0.12 V/m. Based on ITER Basis published in 2007, Breakdown in ITER will employ 2MW EC-assist scenario to ensure a reliable breakdown with marginal range. In Fig. 3-4, it also shows a poloidal magnetic flux configuration of field-null in ITER. Fundamental ECR layer of 127GHz is located at the field-null in order to support the breakdown and current ramp-up phase.

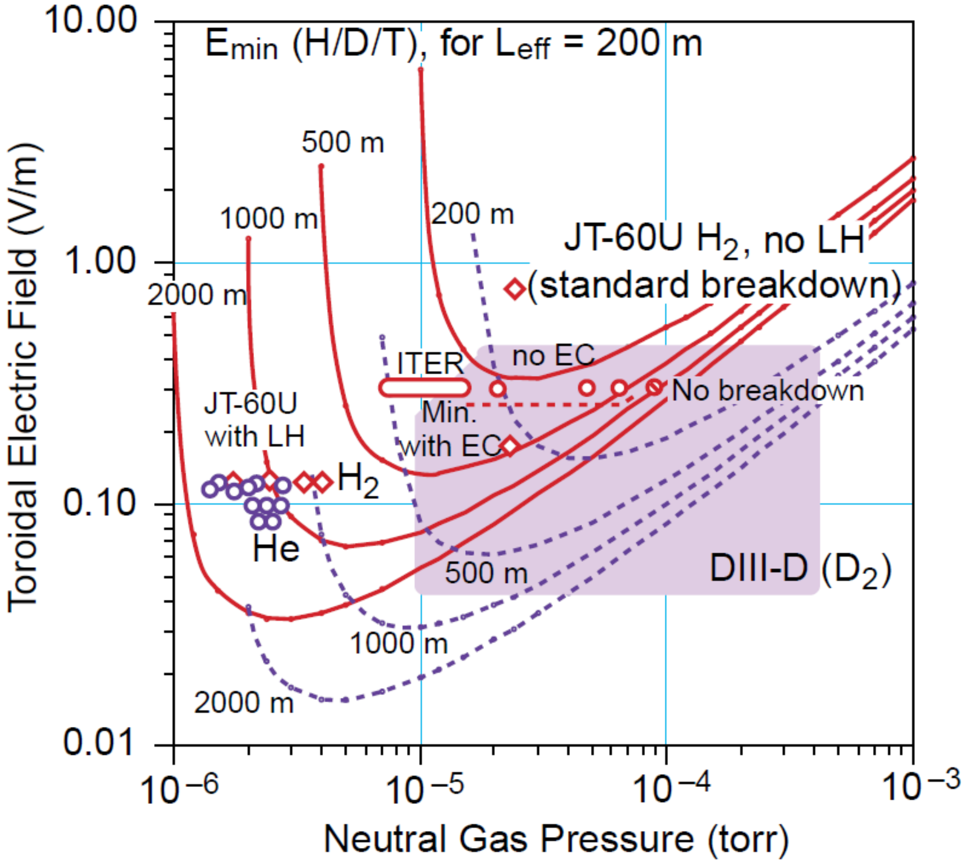

Fig. 3-3. Minimum electric fields for Townsend avalanche breakdown in hydrogen, deuterium or tritium and in helium (dashed lines), for various connection lengths. (Reprinted from Ref. 3)

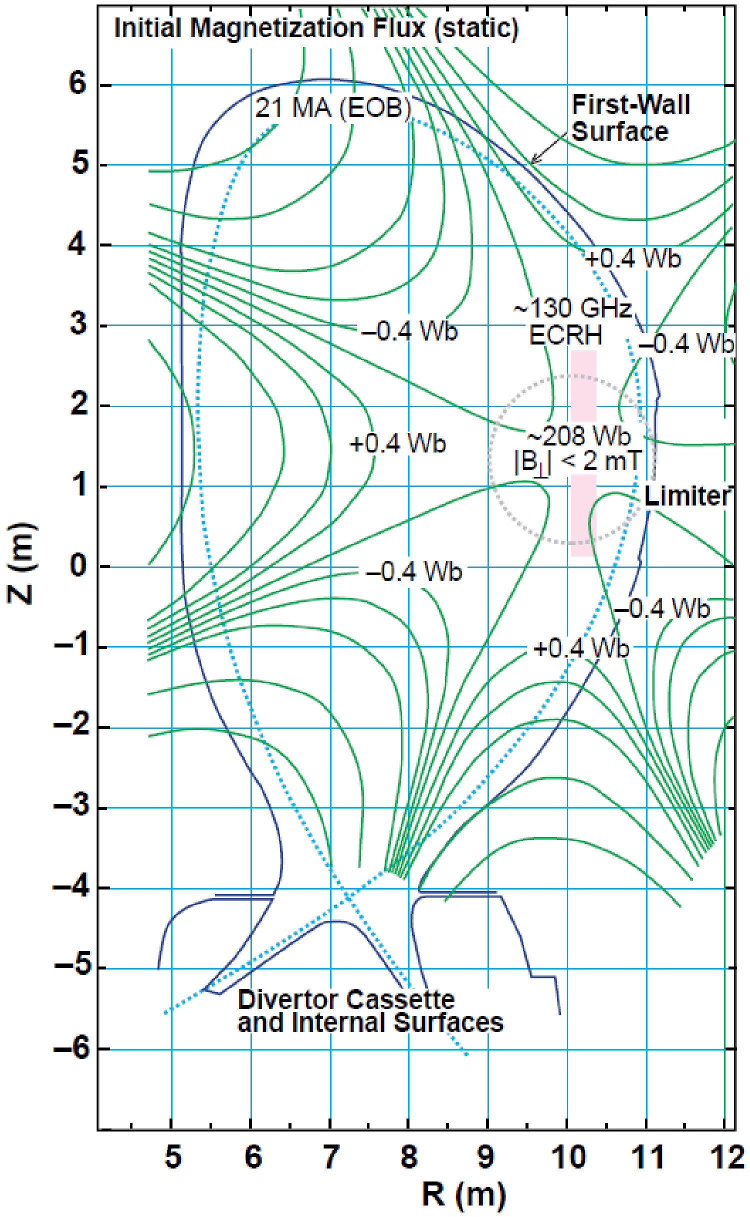

Fig. 3-4. Plasma initiation and current ramp up configurations in ITER (Reprinted from Ref. 3)

3.2 RF-induced Breakdown

In previous section, loss schemes of breakdown phase in tokamak configuration are specified and experimental evidence for ITER that RF injection sufficiently reduces the required E_{min} is denoted. The reason of the reduction of E_{min} is that RF heating of plasma raises plasma density and temperature beforehand, therefore, this is called pre-ionization. Pre-ionization does not mean that it causes breakdown, however, RF injection itself can realize breakdown without Ohmic[7,8].

RF-induced breakdown is very attractive for ST devices since they have no space for CS technically and is the main topic of this doctoral thesis. ECRH as one of non-inductive heating methods has been intensively studied in STs with external vertical field: MAST[9], CDX-U[10], LATE[11], TST-2[12], VEST[13] and QUEST[14–16]. Conventional breakdown with Ohmic usually requires a long connection length (typically 200-2000m) by making use of field-null. On the other hand, RF-induced breakdown is possible with very shorter connection length with no field-null. In QUEST, breakdown with ~ 4.0 m has been reported[17]. This is quite different from Ohmic breakdown and, for the first, we describe the mechanism of ECH breakdown.

In the chapter 2, we see that electrons get a kick in the perpendicular direction to magnetic field at ECR layer. On the other hand, in Ohmic heating, electrons are accelerated in the direction parallel to magnetic field. This difference would change the loss scheme in the breakdown phase. Recall that in Eq. 3.8, we assume that after some collisions electrons obtain a constant velocity of v_{direct}. This assumption is no longer valid in RF-induced breakdown. At ECR layer, electrons are heated by the EC field on the plane of cyclotron motion and thermalized electrons start to diffuse along with magnetic line of force[18]. Ambipolar diffusion takes place in the direct loss scheme and the diffusion velocity is governed by ion sound velocity,

$$C_{\mathrm{s}} = \sqrt{k_{\mathrm{B}} T_{\mathrm{e}} / m_{\mathrm{i}}} \qquad 3.11$$

where k_{B} is Boltzmann's constant and m_{i} is the ion mass. A physical picture of ambipolar diffusion can be written as following. First, electrons heated by ECRH start moving along with the line of force due to higher mobility compared to ions, but the electric field formed between electrons and ions try to decelerate electrons and to accelerate ions. As a consequence, they diffuse together at the same speed. Here, the temperature of electrons must be much larger than that of ions, which is suitable description for ECRH. RF-induced breakdown modeling in chapter 5 constitutes a model based on the discussion above and some quantitative values are specified.

There are considerable experimental results in comparison of breakdown difference between X-mode and O-mode injections. Early results in WT-1[19] showed that the effect of X-mode and O-mode pre-ionization were the same since the mode polarity was lost through RF multi-reflection inside the vessel. More specifically in TCA[20], breakdown comparison in X-mode and O-mode from the HFS were investigated. RF was launched from the top side of the torus and reflected at a stainless mirror to realize HFS injection at frequency of 39GHz and power up to 125kW. Their experiments showed remarkable difference in X and O-mode breakdowns. Visible emission (Ha) from X-mode injection was much localized at UHR not at ECR, this suggests that the mode conversion to EBW occurs and dominates the heating mechanism. In contrast, O-mode injection showed a broader emission between UHR and ECR. This is because O-mode does not see the R-cutoff and pass through the resonances with less absorption and multi-reflection takes place. Also with O-mode injection, it produced more impurity flux from the vessel walls than X-mode that RF power was lost to the walls. The plasma density by O-mode was about 60-80% of that produced by X-mode with the same power. For both modes, the first pass absorption is very important factor. HFS X-mode can be largely absorbed at the UHR through EBW conversion. For HFS O-mode, the first absorption can be very weak. Through the multi-reflection process, randomly wave polarizations changes and damped at ECR or UHR. In both cases of wave modes, an important note in this TCA study was that the UHR dominates heating once the lowest density plasma created.

3.3 Non-linear Power Absorption with ECRH

In Chapter 2, we discussed that the optical thickness $\Gamma(\mathrm{X,O})$ assumes the presence of plasma density and temperature and is no longer valid before the breakdown of plasma. In this section, non-linear power absorption to evaluate breakdown phase is presented. For this purpose, we consider a single electron passing the ECR surface. From the Eq. 2.37 and 2.38, if we assume $q = (\omega_{pe}/\Omega_{\mathrm{ce}})^2 < 0.01$ in the low-density regime, $\Gamma(\mathrm{X,O})$ is evaluated in Fig. 3-5. Showing that X-mode contribution is always very much superior to O-mode absorption. Now and then, X-mode illumination to a single electron in a transit of ECR layer is discussed. Based on a discussion by G. Guest[21], an electron interaction with X-mode after a transit of the fundamental ECR can be described by

$$\Delta W_{\perp} = -e\sqrt{2}|E_{-}|v_{\perp}(0)J_0^2(k_{\perp}\rho)t_{eff}\cos\phi_{res} + \left(\frac{e^2}{m_e}\right)|E_{-}|^2 J_0^2(k_{\perp}\rho)t_{eff}^2, \qquad 3.12$$

where $\Delta W_{\perp}$ is the perpendicular energy gained or lost during one transit, E_{-} is the right-hand circularly polarized component that resonates with electron cyclotron motion, $v_{\perp}(0)$ is the initial perpendicular velocity, t_{eff} is the effective duration of resonance and ϕ_{res} is the stationary value of the phase difference between electron gyration and E_{-} of RF. The first term on the right has a component of ϕ_{res}. It will disappear when averaged over a population of electrons containing random gyro-phases. As a result, the second terms remains and is always positive. The usefulness of this analysis comes from a fact that an evaluation of very low temperature electrons (room temperature $T_e{\sim}0.03$eV) is possible. Before the breakdown, we can assume that a few electrons ionized by space X-ray exist inside the vacuumed chamber.

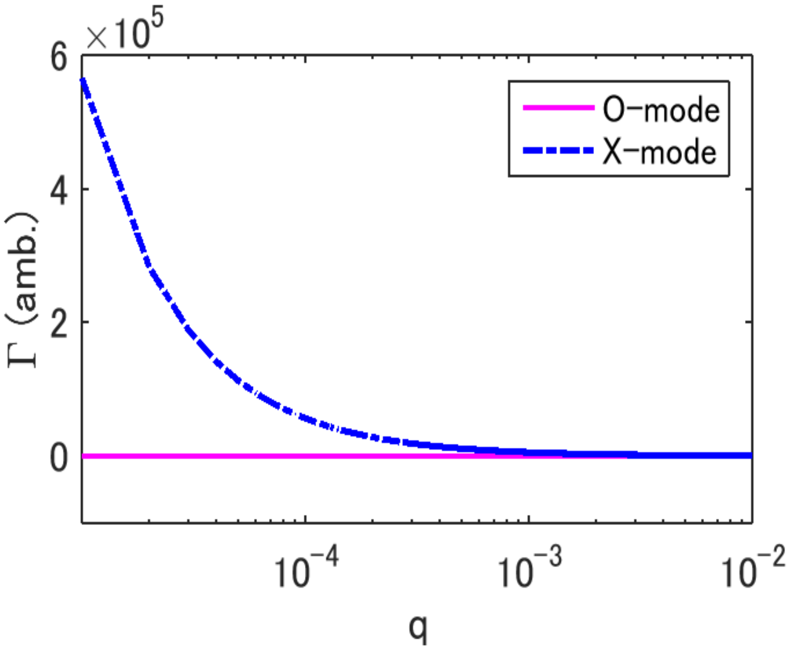

Fig. 3-5. The optical thickness $\Gamma(\mathrm{X},\mathrm{O})$ in the range of $q = (\omega_{pe}/\Omega_{\mathrm{ce}})^2 < 0.01$. Other parameters such β_e, R_0 and λ_0 are fixed.

In Eq. 3.12, we ignored the relativistic effect. To evaluate precisely the non-linear interaction of X-mode and electrons, we borrow a technique developed by M. D. Carter *etc*[22–24]. Again, the Lorentz equation of electrons and RF electromagnetic field,

$$\frac{d(\gamma m_0 \boldsymbol{v})}{dt} = -e(\boldsymbol{v} \times \boldsymbol{B} + \boldsymbol{E}) \qquad 3.13$$

where

$$\gamma = \left(1 - \frac{\boldsymbol{v} \cdot \boldsymbol{v}}{c^2}\right)^{-\frac{1}{2}} \qquad 3.14$$

is the relativistic effect and m_0 is the electron rest mass. The notation of $\boldsymbol{E}$ as,

$$\boldsymbol{E} = E_x \hat{x} \sin(kx - \omega t) + E_y \hat{y} \cos(kx - \omega t). \qquad 3.15$$

The system considered is denoted in Fig. 3-6. ψ is the phase of electron's cyclotron motion. RF wave polarization is X-mode by taking the static magnetic field lies in the z direction. By setting,

$$v_x = -v_\perp \sin\psi, v_y = v_\perp \cos\psi, x = \rho \cos\psi \qquad 3.16$$

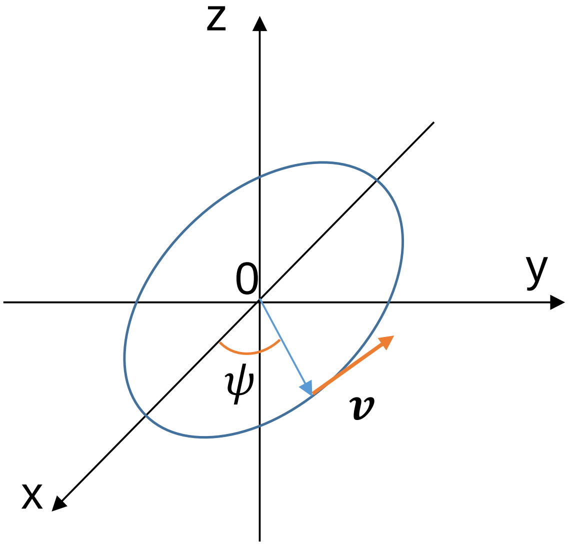

Fig. 3-6. The coordinate used in analysis. RF wave propagation is on

the Lorenz equation (Eq. 3.13) becomes and manipulating,

$$\frac{d\psi}{dt} = -\frac{eB}{\gamma m_0} + \frac{eE_0}{2\gamma m_0 v_\perp}\sin[k\rho\cos\psi - \omega t + \psi] \tag{3.17}$$

$$\frac{d\gamma}{dt} = -\frac{ev_\perp E_0}{2m_0c^2}\cos[k\rho\cos\psi - \omega t + \psi] \tag{3.18}$$

$$\boldsymbol{E} = \frac{E_0}{2}\{\sin[k\rho\cos\psi - \omega t]\hat{x} + \cos[k\rho\cos\psi - \omega t]\hat{y}\} \tag{3.19}$$

Here we assume very low electron temperature that $k\rho \ll 1$. This corresponds the condition for plasma breakdown that the Larmor radius is much shorter than the wavelength of RF. Under the condition, we can take $k\rho \sim kv_\perp/\Omega_{\mathrm{ce}} \sim v_\perp/c$. Here, we define new notations, $\Psi \equiv n\psi - \omega t$ and $\Theta \equiv \gamma - 1$. n is the harmonic number and Ψ stays constant in non-relativistic case at ECR but in relativistic case, it changes with time. We can also understand that Θ is the ration of the kinetic energy of electrons to the rest electron's mass energy m_0c^2. At our convenience, we define a dimensionless term; $\varepsilon \equiv eE/m_0c\omega$. Based on the introduced variables, the equations above can be modified, for $n =$ even,

$$\frac{d\Psi}{dt} = -\Theta\omega - \frac{\varepsilon\omega}{(n-1)!}\left(\frac{n}{2}\right)^{n-1} 2^{\frac{n}{2}-1}\frac{n}{2} \times \Theta^{\frac{n}{2}-1}(-1)^{\frac{n}{2}}\cos\Psi \tag{3.20}$$

$$\frac{d\Theta}{dt} = -\frac{\varepsilon\omega}{(n-1)!}\left(\frac{n}{2}\right)^{n-1} 2^{\frac{n}{2}-1} \times \Theta^{\frac{n}{2}}(-1)^{\frac{n}{2}}\sin\Psi \tag{3.21}$$

and for $n =$ odd,

$$\frac{d\Psi}{dt} = -\Theta\omega + \frac{\varepsilon\omega}{(n-1)!}\left(\frac{n}{2}\right)^{n-1} 2^{\frac{n}{2}-1}\frac{n}{2} \times \Theta^{\frac{n}{2}-1}(-1)^{\frac{n-1}{2}}\sin\Psi \tag{3.22}$$

$$\frac{d\Theta}{dt} = -\frac{\varepsilon\omega}{(n-1)!}\left(\frac{n}{2}\right)^{n-1} 2^{\frac{n}{2}-1} \tag{3.23}$$

$$\times \Theta^{\frac{n}{2}}(-1)^{\frac{n-1}{2}} \cos \Psi$$

The equations from (Eq. 3.20) to (Eq. 3.23) can be combined into,

$$\Theta^2 - 2\varepsilon\alpha\Theta^{\frac{\mathrm{N}}{2}} \cos \Psi = C_1 \qquad N = 2n$$

$$\alpha = -\frac{(-1)^{\frac{N}{2}}}{(n-1)!}\left(\frac{N}{2}\right)^{N-1} 2^{\frac{N}{2}-1} \qquad 3.24$$

$$\Theta^2 - 2\varepsilon\alpha\Theta^{\frac{\mathrm{N}}{2}} \cos \Psi = C_2 \qquad N = 2n+1$$

$$\alpha = -\frac{(-1)^{\frac{N-1}{2}}}{(n-1)!}\left(\frac{N}{2}\right)^{N-1} 2^{\frac{N}{2}-1} \qquad 3.25$$

The constant values of C_1 and C_2 in the resonance zone and are decided by the initial value of electron and the phase difference. Now, we are able to analyze the interaction of electrons and RF wave at each harmonics. For N=1, the fundamental ECR interaction is illustrated as,

$$\Theta^2 - \sqrt{2}\Theta^{\frac{1}{2}}\varepsilon \sin \Psi = C \qquad 3.26$$

Next, for the second harmonics (N=2),

$$\Theta^2 - 2\Theta\varepsilon \cos \Psi = C \qquad 3.27$$

In comparison of fundamental and second harmonics ECRH, we deduce the relation of Ψ and Θ in Fig. 3-7, for example. In Fig.0, there are islands that electrons can be trapped. In the trapping mode, electrons can constantly gain energy during a transit of ECR layer. Moreover, with the fundamental and second X-mode illuminations, the energy transfer to electrons is very different in magnitude. Second harmonic heating is much less efficient than that of the fundamental. We will discuss more in specific in comparison with experimental results in QUEST.

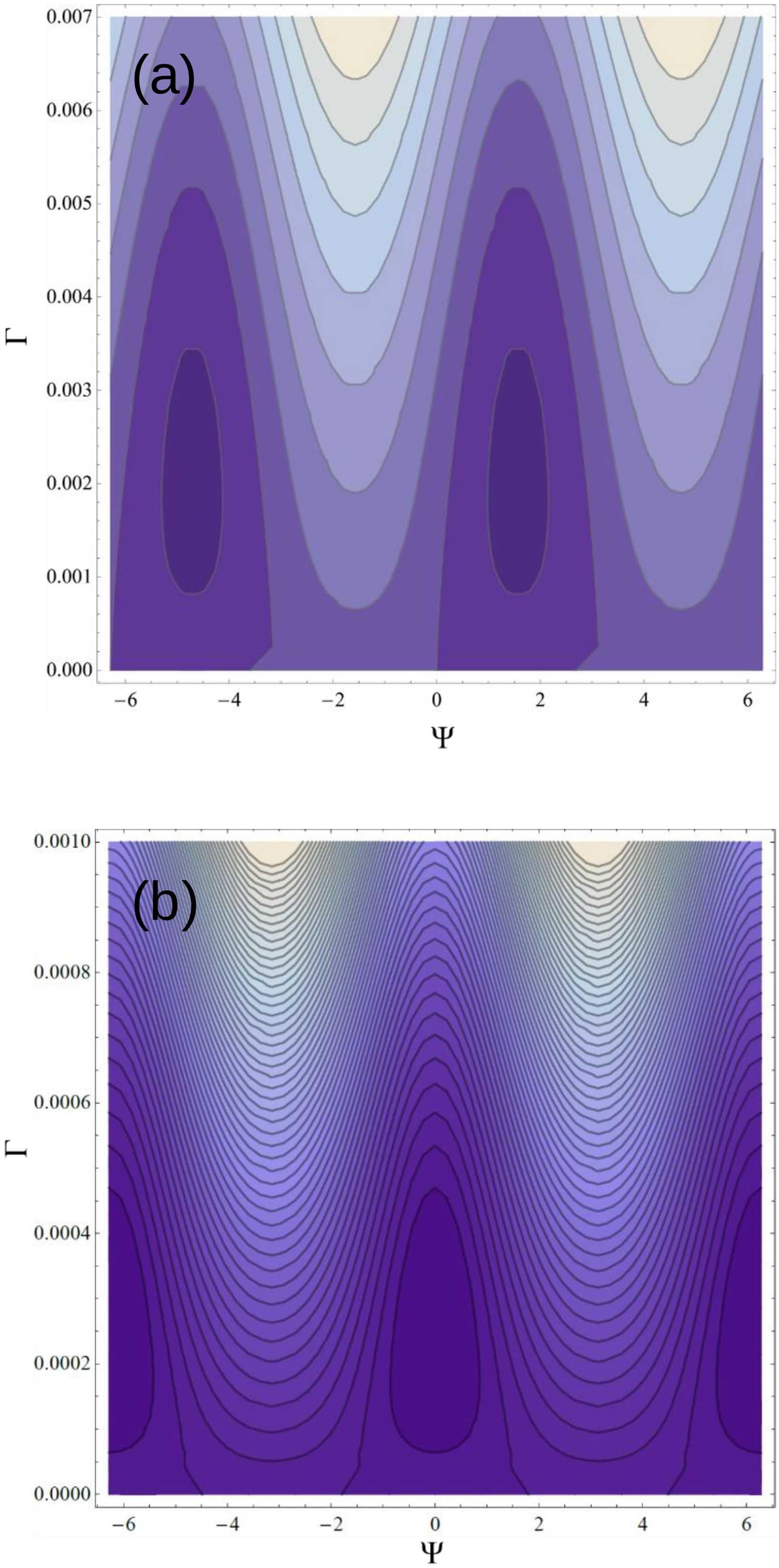

Fig. 3-7. The contour plot of Ψ and Θ with initial $\Theta = 2.67 \times 10^{-4}$. (a) The fundamental ECRH and (b) the second harmonic ECHR.

Refs in Chapter 3

[1] A. Von ENGEL, *Ionized Gases* (Clarendon Press, Oxford, 1965).

[2] A.D. MacDonald and S.C. Brown, Phys. Rev. **75**, 411 (1949).

[3] ITER Physics Expert Groups, Nucl. Fusion **39**, 2577 (1999).

[4] D. Mueller, Phys. Plasmas **20**, (2013).

[5] R. Papoular, Nucl. Fusion **16**, 37 (1976).

[6] B. Lloyd, G.L. Jackson, T.S. Taylor, E. A. Lazarus, T.C. Luce, and R. Prater, Nucl. Fusion **31**, 2031 (1991).

[7] H.J. Oskam, J. Appl. Phys. **27**, 848 (1956).

[8] S. Tanaka, K. Hanada, M. Bornatici, R. Cano, K. Ohkubo, and K. Kawahata, (n.d.).

[9] V.F. Shevchenko, M.R. O’Brien, D. Taylor, and A. N. Saveliev, Nucl. Fusion **50**, 22004 (2010).

[10] C.B. Forest, Y.S. Hwang, M. Ono, G. Greene, T. Jones, W. Choe, M. Schaffer, A. Hyatt, T. Osborne, R.I. Pinsker, C.C. Petty, L. J, and S. Lippmann, Phys. Plasmas **1**, 1568 (1994).

[11] T. Yoshinaga, M. Uchida, H. Tanaka, and T. Maekawa, Nucl. Fusion **47**, 210 (2007).

[12] T. Shinya, Y. Takase, T. Wakatsuki, A. Ejiri, H. Furui, J. Hiratsuka, K. Imamura, T. Inada, H. Kakuda, H. Kasahara, R. Kumazawa, C. Moeller, T. Mutoh, Y. Nagashima, K. Nakamura, A. Nakanishi, T. Oosako, K. Saito, T. Seki, M. Sonehara, H. Togashi, S. Tsuda, N. Tsujii, and T. Yamaguchi, Nucl. Fusion **55**, 73003 (2015).

[13] Y. An, J. Lee, J. Jo, B.K. Jung, H. Lee, K.J. Chung, Y.S. Na, T.S. Hahm, and Y.S. Hwang, Nucl. Fusion **57**, (2017).

[14] K. Hanada, H. Zushi, H. Idei, K. Nakamura, M. Ishiguro, S. Tashima, E.I. Kalinikova, M. Sakamoto, M. Hasegawa, A. Fujisawa, A. Higashijima, S. Kawasaki, H. Nakashima, H. Liu, O. Mitarai, T. Maekawa, A. Fukuyama, Y. Takase, and J. Qian, Plasma Sci. Technol. **13**, (2011).

[15] M. Ishiguro, K. Hanada, H. Liu, R. Ogata, M. Isobe, S. Tashima, H. Zushi, K. Sato, A. Fujisawa, K. Nakamura, H. Idei, M. Sakamoto, M. Hasegawa, Y. Takase, T. Maekawa, Y. Kishimoto, O. Mitarai, S. Kawasaki, H. Nakashima, and A. Higashijima, J. Phys. Conf. Ser. **511**, 12041 (2014).

[16] S. Tashima, H. Zushi, M. Isobe, K. Hanada, H. Idei, K. Nakamura, A. Fujisawa, K. Matsuoka, M. Hasegawa, Y. Nagashima, S. Okamura, S. Banerjee, S. Kawasaki, H. Nakashima, and a. Higashijima, Nucl. Fusion **54**, 23010 (2014).

[17] R. Bhattacharyay, H. Zushi, T. Morisaki, Y. Inada, T. Kikukawa, S. Watanabe, K. Sasaki, T. Ryoukai, M. Hasegawa, K. Hanada, K.N. Sato, K. Nakamura, M. Sakamoto,

H. Idei, T. Yoshinaga, S. Kawasaki, H. Nakashima, and A. Higashijima, Phys. Plasmas **15**, (2008).

[18] S. Nakao, K. Ogura, Y. Terumichi, and S. Tanaka, Phys. Lett. A **96**, 405 (1983).

[19] T. Ocho, S. Kubo, M. Ikeda, T. Saito, Y. Terumichi, Y. Hamada, and S. Tanaka, Phys. Lett. A **77**, 318 (1980).

[20] D.R. Whaley, T.P. Goodman, A. Pochelon, R. Behn, A. Cardinali, B.P. Duval, B. Joye, and M.Q. Tran, Nucl. Fusion **32**, 757 (1992).

[21] G. Guest, *Electron Cyclotron Heating of Plasmas* (Wiley-VCH, 2009).

[22] M.D. Carter, J.D. Callen, D.B. Batchelor, and R.C. Goldfinger, Phys. Fluids **29**, 100 (1986).

[23] J. Seol, C.C. Hegna, and J.D. Callen, Phys. Plasmas **16**, (2009).

[24] J.C. Seol, B.H. Park, S.S. Kim, J.Y. Kim, and Y.S. Na, Nucl. Fusion **50**, 0 (2010).

4. QUEST Apparatus

Q-shu University Experiment with Steady-State Spherical Tokamak (QUEST) is a medium-sized ST at Kyushu University[1]. Outer diameter of the vacuum vessel is 2.74 m, inner diameter is 0.44 m and its height is 2.8 m as shown in Fig. 4-1. A pair of toroidal coils is set at every 45 degrees in toroidal direction and total 16 toroidal coils penetrate central column of the vessel. Steady current up to 50 kA is now available and toroidal field of 0.25T is provided at the center of the chamber, major radius R = 0.64 m. 11 poloidal field coils and a pair of cancel coils generate poloidal magnetic field. Each PF coil forms a pair with a coil set in symmetric position of it, for example PF1 and PF7 coils, and a pair of coils is connected to one electric power supply in series. PF1/PF7 and PF2/PF6 coils are mainly used to keep a tokamak plasma equilibrium and PF3/PF5 coils are used for making diverter configuration.

As for RF system, one 2.45 GHz system up to 50 kW, and one 8.2 GHz Klystron systems up to 200 kW. 28 GHz Gyrotron up to 450kW is also installed. Also in Fig. 4-1, flat diverter plates on which tungsten was sprayed to endure high heat load are located at ±1m from the mid-plane. A Langmuir probe array is located in radial direction on the upper diverter plate (See Fig. 4-2). It forms triple-probe to measure electron temperature and electron density at the same time. The curvature of poloidal field defined as n-index,

$$n = -(R/B_\mathrm{v}) \cdot (\partial B_\mathrm{v}/\partial R). \qquad 4.1$$

it can be arranged to arbitral values by controlling the ratio of each coil current. B_v is the vertical magnetic field.

Experiments of fundamental 2.45 GHz and 8.2 GHz were performed with different n-index configuration by controlling PF coils: positive and negative n-index configuration. Typical magnetic structures used in the experiments are shown in Fig. 4-3. RF waves injected from both RF systems were propagating as O-mode in the experiments. The hydrogen molecule neutral pressure can be controlled with a mass flow meter (Model No.MQV9020). In these experiments, connection length L is defined as the length of magnetic lines of force from the mid-plane at the ECR layer to the intersection with divertor plate. Throughout the experiments, the fundamental ECR layer was fixed at R = 532 mm for 2.45 GHz and R = 545 mm, respectively. That is, controlling toroidal magnetic field B_TF to 0.087 T and 0.29 T at ECR layer, respectively for 2.45 GHz and 8.2 GHz. The PF coils current has a certain range of tolerance that the error of L cannot be avoidable. Since $L \propto B_\mathrm{TF}/B_\mathrm{v}$, error range of 2.45 GHz becomes larger than 8.2 GHz. They were ±20 m and ±3 m respectively.

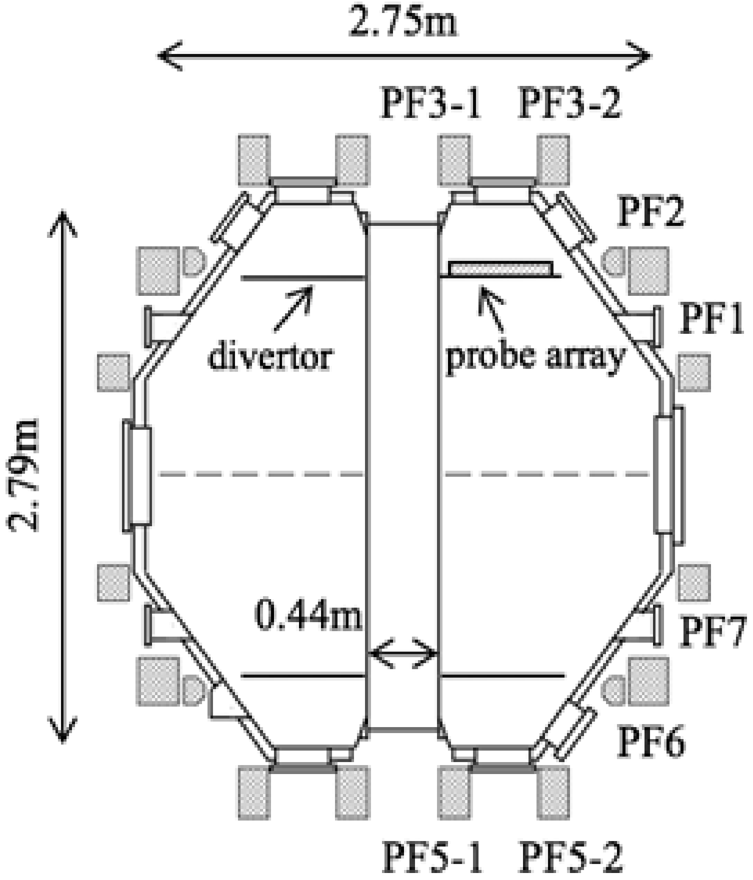

Fig. 4-1. The cross-sectional view of QUEST vessel and the position of PF coils and divertor probe array.

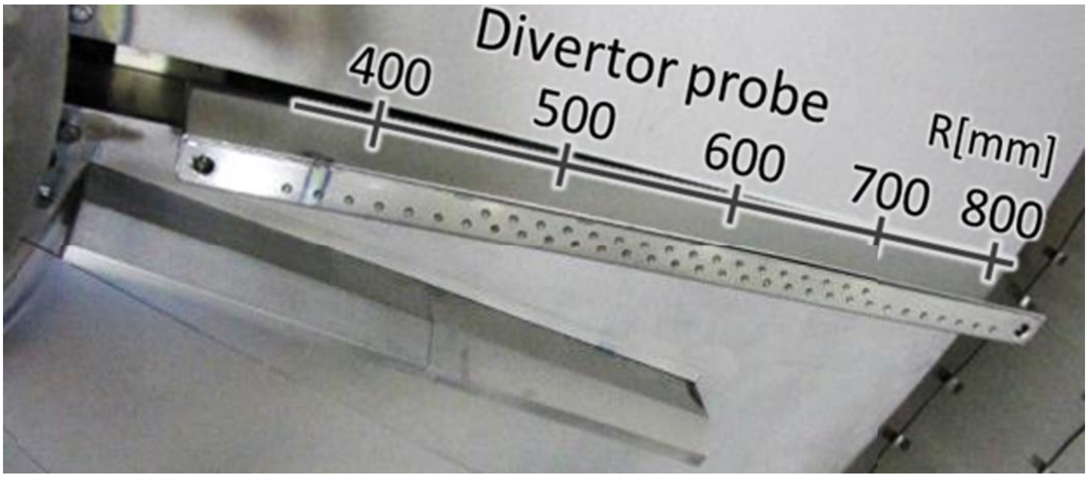

Fig. 4-2. Location of the probe array on the upper divertor plate. It forms triple-probe from R = 460 to 700 mm.

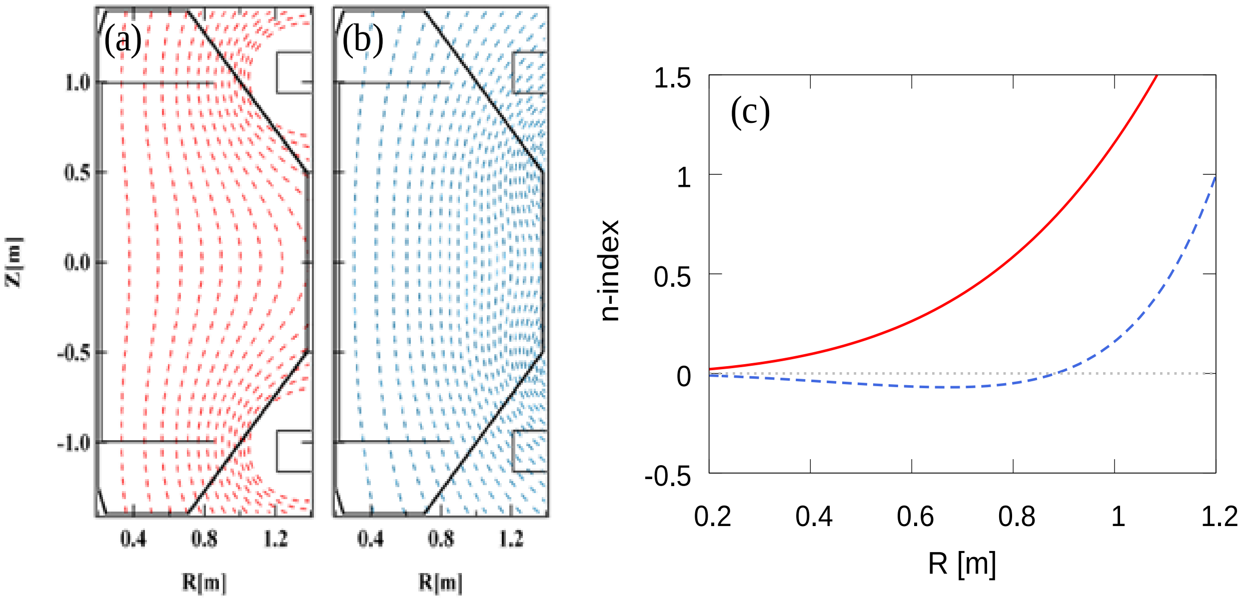

Fig. 4-3. Typical magnetic flux structure in the cases of (a) positive and (b) negative *n*-index. PF2/PF6 coils for positive and PF1/PF7 coils for negative *n*-index are in use respectively. (c) n-index calculated at mid-plane (Z=0) for both cases. Solid line stands for positive *n*-index and dashed line for negative *n*-index..

4.1 Langmuir Probe

Langmuir probes are widely applicable from laboratory plasma to space plasma[2]. It can provide electron temperature T_e and density n_e. Characteristic of the current-potential curve is shown in Fig. 4-4, where ϕ_w is the negative floating potential. T_e can be obtained by evaluating the slope of the curve (red line in Fig. 4-4). That is,

$$T_\mathrm{e} = \frac{e}{k}(\frac{d}{d\phi}[\ln(J_p + J_i)])^{-1}, \qquad 4.2$$

where the current density of the probe can be written as in the range of $\phi < 0$,

$$J_p = J_{e0}\exp(\frac{\mathrm{e}\phi}{kT_e}). \qquad 4.3$$

If we have the value of T_e, n_e can be derived by using electron saturation current $J_{\mathrm{e}0}$,

$$n_\mathrm{e} = \frac{J_{e0}}{e}(\frac{2\pi m_e}{kT_e})^{\frac{1}{2}}, \qquad 4.4$$

Note that the triple probes used during the experiments can provide T_e and n_e at the same time.

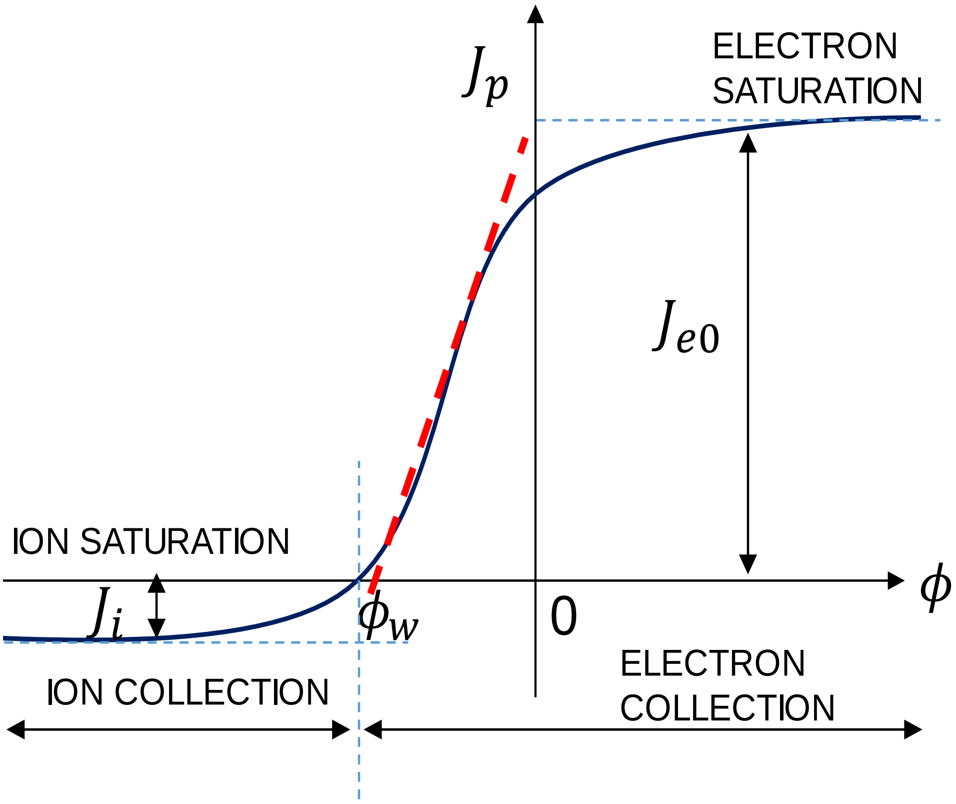

Fig. 4-4. Characteristic of the current-potential curve of Langmuir probe.

4.2 Ha Emission from Hydrogen Plasma

The Ha signal is a line spectrum of Balmer series, which wave length $\lambda = 656.28\mathrm{nm}$. The Ha spectrum is a result of when an excited electron of hydrogen atom at n = 3 fells into n = 2. Here, n is the number of energy level of hydrogen atom. We use this signal to determine whether breakdown is obtained or not. The reason why Ha signal is a measure of breakdown can be explained as follows. Electron avalanche, breakdown of plasma, causes electron and ion density build-up and at the same time hydrogen neutrals $(\mathrm{H}\ \text{and}\ \mathrm{H}_2)$ are consumed. Since excitations are possible with lower T_e than $T_e = 13.6\mathrm{eV}$, which is ionization energy of hydrogen, Ha signal shines bright in the breakdown phase. Note that we assume here that all particles have Maxwellian profiles.

Refs in Chapter 4

[1] K. Hanada, K. Sato, H. Zushi, K. Nakamura, M. Sakamoto, H. Idei, M. Hasegawa, and Y. Takase, Plasma Fusion Res. **5**, 1 (2010).

[2] H.M. Mott-Smith and I. Langmuir, Phys. Rev. **28**, 727 (1926).

5. Particle and Energy Balance Equation Development of Hydrogen Plasma

In requirement of breakdown modeling, this chapter describes development of particle and energy balance equations of hydrogen plasma. The aim of this modeling is to simulate the plasma build-up as a consequence of electron avalanche. In start-up phase where plasma temperature remains low, we need to take care of partially ionized gas[1]. Therefore, the model developed includes not only ionization but also recombination and excitation of hydrogen particles[2–4].

5.1 Particle Balance Equations

Firstly, we discuss the development of particle balance equations. Depending on the database, we can obtain reaction rate of each reaction shown on Table 5-1. Figure 5-1 is the reaction rate from the database[5]. The particle balance equations[6–8] are denoted as

$$\frac{dn_p}{dt} = \sum_{j<k} \sum_{i} \epsilon_{jkp}^{i} k_{jk}^{i} n_j n_k - \frac{n_p}{\tau_{\mathrm{loss}}}, \qquad 5.1$$

where, ϵ_{jkp}^{i} is the number of lost or gained by the reactions, k_{jk}^{i} is reaction rate for reaction i between j and k, n_p is population density. The first term of the right-hand side of the equation stands for the production and disappearance of particles and the second is the loss term represented by τ_{loss}. It solves the time evolution of simultaneous differential equation of each reaction of hydrogen. When considering the particle loss of ECR plasma with vertical magnetic field, there should be drift loss ($\tau_{\mathrm{loss}\perp}$) and loss along with magnetic lines of force ($\tau_{\mathrm{loss}\parallel}$). When connection length L gets longer, drift loss (curvature and grad B drift) becomes dominant. In the experimental regime in this paper, loss mechanism is governed by the loss along magnetic lines of force. It was also described that the dominant particle loss during the breakdown phase mainly comes from the direct loss along magnetic lines of force, and that is,

$$\tau_{\mathrm{loss}} = \frac{L}{v_{\phi}}, \qquad 5.2$$

where v_{ϕ} is the velocity of electrons along with magnetic lines of force. In Chapter 3, we showed that the accelerated electrons at ECR layer by RF wave are assumed to be governed by ambipolar diffusion, and this mechanism leads to the fact that electrons practically move along magnetic lines of force at the ion sound velocity C_s,

$$C_s = \sqrt{k_{\mathrm{B}} T_{\mathrm{e}} / m_{\mathrm{i}}}, \qquad 5.3$$

where, k_{B} is the Boltzmann's constant, T_{e} is the electron temperature and m_{i} is the ion mass. By introducing the loss term due to electron movement parallel to the magnetic field, the point model of hydrogen ionization is modified. For the electron density, the particle balance equation is described as,

$$\frac{dn_{\mathrm{e}}}{dt} = \sum_{j<k} \sum_{i} \epsilon_{jkp}^{i} k_{jk}^{i} n_j n_k - \frac{n_e C_s}{L}, \qquad 5.4$$

The calculation requires the initial values of electron density and hydrogen molecule density. The measured values from divertor probe are used. Note that T_{e} plays roles in both production and loss of plasma particles. Higher T_{e} is preferable for ionization but it enhances loss term by increasing C_s at the same time. In this manner, L should be one key parameter for breakdown.

Table 5-1. Reactions between hydrogen particles and electrons in the model.

	Electron Collisions with H, H^+	
R1[a]	Excitation	$\mathrm{e} + \mathrm{H} \rightarrow \mathrm{e} + \mathrm{H}^*(n = 2,\ 3)$
R2	Ionization	$\mathrm{e} + \mathrm{H} \rightarrow \mathrm{e} + \mathrm{H}^+ + \mathrm{e}$
R3	Recombination	$\mathrm{e} + \mathrm{H}^+ \rightarrow h\nu$
	Electron Collisions with H_2, H_2^+ and H_3^+	
R4	Dissociation	$\mathrm{e} + \mathrm{H}_2 \rightarrow \mathrm{e} + \mathrm{H} + \mathrm{H}$
R5	Ionization	$\mathrm{e} + \mathrm{H}_2 \rightarrow \mathrm{e} + \mathrm{H}_2^+ + \mathrm{e}$
R6	Dissociative Ionization	$\mathrm{e} + \mathrm{H}_2 \rightarrow \mathrm{e} + \mathrm{H}^+ + \mathrm{H} + \mathrm{e}$
R7	Dissociation	$\mathrm{e} + \mathrm{H}_2^+ \rightarrow \mathrm{e} + \mathrm{H}^+ + \mathrm{H}$
R8	Dissociative Recombination	$\mathrm{e} + \mathrm{H}_2^+ \rightarrow \mathrm{H} + \mathrm{H}$
R9	Dissociative Recombination	$\mathrm{e} + \mathrm{H}_3^+ \rightarrow \mathrm{H}_2 + \mathrm{H}$
R10	Dissociation	$\mathrm{e} + \mathrm{H}_3^+ \rightarrow \mathrm{e} + \mathrm{H}^+ + \mathrm{H} + \mathrm{H}$
	Ion Impact Reactions	
R11	Charge Exchange	$\mathrm{H}^+ + \mathrm{H} \rightarrow \mathrm{H} + \mathrm{H}^+$
R12	H_3^+ Formation	$\mathrm{H}_2 + \mathrm{H}_2^+ \rightarrow \mathrm{H}_3^+ + \mathrm{H}$
R13	Ionization	$\mathrm{H}^+ + \mathrm{H} \rightarrow \mathrm{e} + \mathrm{H}^+ + \mathrm{H}^+$

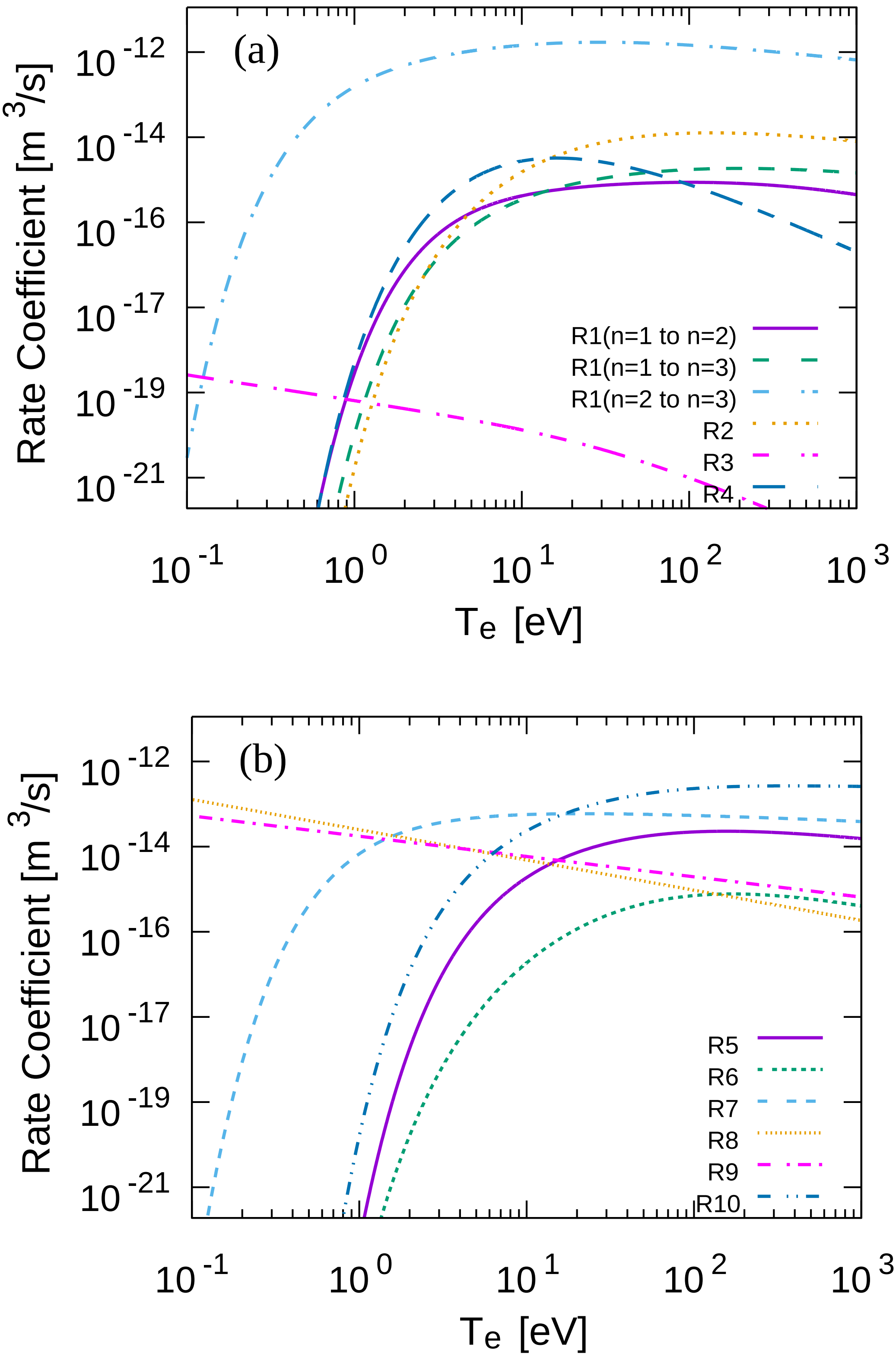

Fig. 5-1. The rate coefficients for hydrogen particle reactions on Table 5-1. (a) Reaction R1 to R4. (b) Reaction R5 to R10.

5.2 Energy Balance Equations

Inclusion of energy balance equations enables an analysis that bridges the injected RF power and the plasma production and loss. A set of energy balance equations can be written as,

$$\begin{aligned}\frac{3}{2}\frac{dn_pT_p}{dt} &= \frac{dE_p}{dt}\\ &= \sum_{j<k}\sum_{i}\epsilon^i_{jkp}E^i_{jkp}k^i_{jk}n_jn_k \\ &+ \sum_j E_{jp}k^{\mathrm{el}}_j n_j n_p - \frac{3}{2}\frac{n_pT_p}{\tau_{E,p}} + P_{\mathrm{RF},p},\end{aligned} \tag{5.5}$$

where, T_p is the Maxwellian temperature of particles, E^i_{jkp} is the energy transferred for each corresponding reaction, τ_E is the energy relaxation time, E_{jp} is the energy transferred due to elastic collisions, k^{el}_j is the elastic collision reaction rate and P_{RF} is the RF power absorbed to plasma particles. The left hand side of the equation tells that the energy balance equations involve the time evolution plasma density and temperature. In this way, if sufficient energy input provided, one would obtain an energy equilibrium point. The first term of the right hand side corresponds to the inelastic collisions of particles. The second stands for the elastic collisions and the third is for energy confinement. The fourth term of P_{RF} is the input source of the plasma sustainment. For the evaluation of coupling power to the plasma, we must consider wave absorption profiles

Refs in Chapter 5

[1] R.K. Janev, D. Reiter, and U. Samm, Sci. York 190 (2003).

[2] D. Wünderlich, S. Dietrich, and U. Fantz, J. Quant. Spectrosc. Radiat. Transf. **110**, 62 (2009).

[3] J. Liu, E.J. Salumbides, U. Hollenstein, J.C.J. Koelemeij, K.S.E. Eikema, W. Ubachs, and F. Merkt, J. Chem. Phys. **130**, 1 (2009).

[4] K. Hassouni, T.A. Grotjohn, and A. Gicquel, J. Appl. Phys. **86**, 134 (1999).

[5] J. R.K. Janev, W.D. Langer, K. Evans & Jr, D.E. Post, *ELEMENTARY PROCESSES IN HYDROGEN-HELIUM PLASMAS* (Springer-Verlag, Berlin, 1987).

[6] T. Wauters, a Lyssoivan, D. Douai, O. Marchuk, D. Wünderlich, R. Koch, G. Sergienko, G. Van Oost, and M. Van Schoor, Plasma Phys. Control. Fusion **53**, 125003 (2011).

[7] R. Yoneda, K. Hanada, K. Nakamura, H. Idei, N. Yoshida, M. Hasegawa, T. Onchi, K. Kuroda, S. Kawasaki, A. Higashijima, T. Nagata, A. Isayama, O. Mitarai, A. Fukuyama, and Y. Takase, Cit. Phys. Plasmas **24**, (2017).

[8] Y. V Ralchenko and Y. Maron, J. Quant. Spectrosc. Radiat. Transf. **71**, 609 (2001).

6. Experimental Results of RF-induced Plasma Breakdown

RF-induced breakdown experiments in QUEST have been demonstrated to investigate RF-oriented breakdown mechanism. In this chapter, experimental conditions are specified and discussion on RF-induced breakdown with the one-point model is presented[1].

6.1 Comparison of Magnetic Structure: Negative and Positive n-index

The experiments of RF-induced breakdown were carried out with two different RF frequencies of 2.45GHz and 8.2GHz. First of all, the typical waveforms, where we have breakdown and no breakdown are shown in Fig. 6-1. After making sure that parameters such as the toroidal field coil current I_{TF}, the poloidal field coil current I_{PF} and hydrogen pressure p_{neutral} reach constant values, RF power injection takes place in order to attain reproducibility. For conducting experiments efficiently, we made RF power modulations that RF was injected 5 times each at the same power and seamlessly changed to different levels. For example, RF modulations to 3kW, 6kW and 12kW for 2.45 GHz and to 10 kW, 15 kW and 20 kW for 8.2 GHz. The Hα signal tells that we have a breakdown or not (see Fig. 6-1(a)). Throughout the experiments, p_{neutral} was controlled by mass flow meter and stays in a range of $p_{\mathrm{neutral}} = 3.0 \sim 6.0\times10^{-3}$ Pa. p_{neutral} was measured by an ion gauge. In case of negative n-index, the dependence on magnetic connection length L by with different RF injection power is shown in Fig. 6-2. Both for 2.45 GHz and 8.2 GHz, there were no effects on the RF injection power, however, clear thresholds of breakdown existed on L. They were 110 m for 2.45 GHz and 85 m for 8.2 GHz respectively. The minimum RF power were 3 kW for 2.45 GHz and 2kW for 8.2 GHz. In these conditions, one can estimate that the direct loss along magnetic lines of force was superior, and the breakdown conditions were highly sensitive with L. For the RF frequency used in the experiments, drift loss becomes dominant above $L \sim 150$ m and 500 m for 2.45 GHz and 8.2 GHz, respectively. It has a relation to the cyclotron frequency as drift velocity v_{drift} and loss duration τ_{drift} are expressed: $v_{\mathrm{drift}} = \frac{1}{R\omega_{\mathrm{ce}}}\left(\frac{1}{2}v_{\perp}^2 + v_{\parallel}^2\right)$ and $\tau_{\mathrm{drift}} = b/v_{\mathrm{drift}}$, where R_{ECR} is the location of ECR layer, ω_{ce} is cyclotron frequency, $v_{\perp}^2 \sim v_{\parallel}^2 \sim 3k_{\mathrm{B}}T_{\mathrm{e}}/2m_{\mathrm{e}}$ is thermal velocity, and b is vertical minor radius. The estimation above is calculated: R =540 mm, T_{e} = 5 eV, and b = 1 m. This suggests that the higher frequency suppresses the drift loss, or equivalently, a strong magnetic field induction does the same.

On the other hand, for positive n-index, there were no dependence on both RF injection power and L, and breakdown was always obtained (see Fig. 6-3). For positive n-index cases, the effective connection length for the electron loss becomes longer than the connection length of the magnetic lines of force because of the presence of closed electron orbit in the positive n-index configuration[2,3]. In other words, a lifetime of incubated electrons is very much important for breakdown that a sufficient lifetime of electrons enables Townsend avalanche of electrons. As for negative n-index, we can assume that the lifetime is only governed by L on which electrons escape, therefore, breakdown conditions become sensitive for L. These results clearly indicate that positive n-index configuration is a desirable method to acquire RF-induced breakdown.

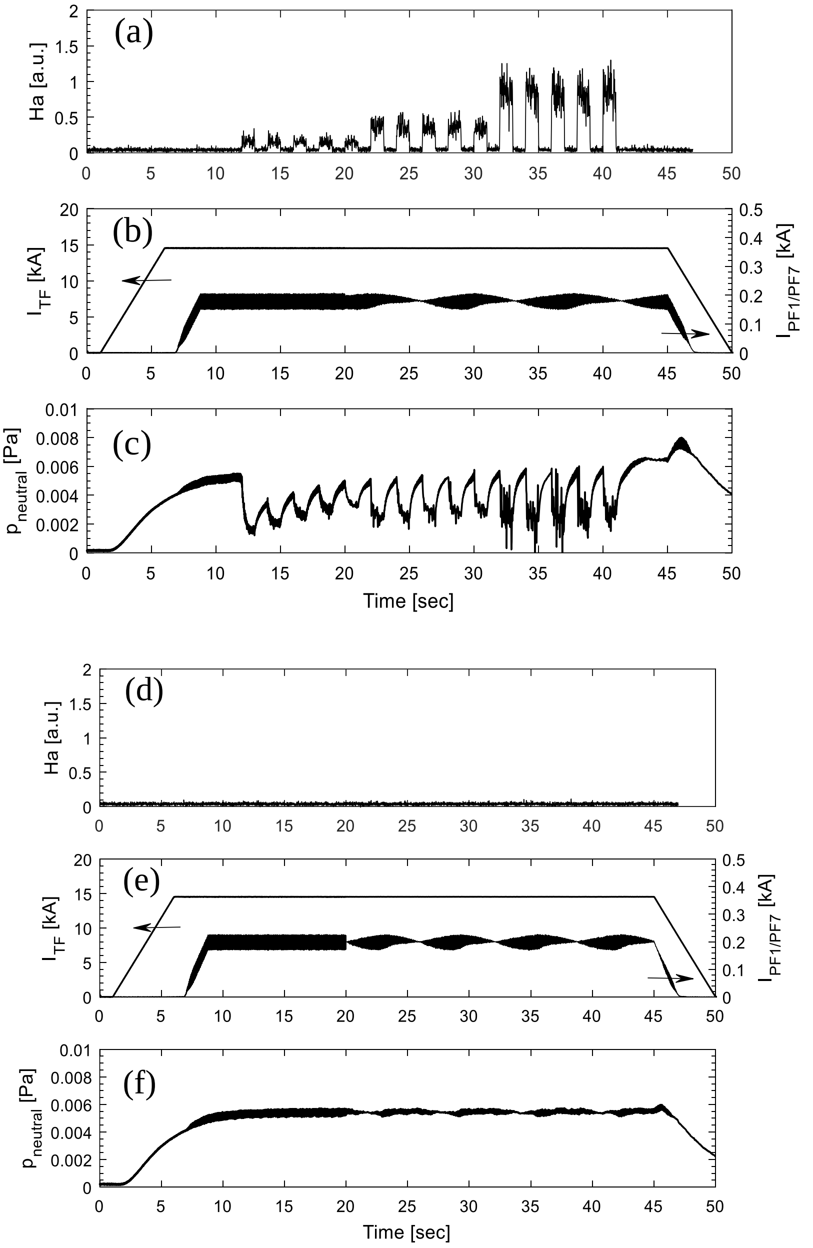

Fig. 6-1. Waveforms of typical shots for 2.45GHz with breakdown (a, b, c) and no breakdown (d, e, f) with negative *n*-index. (a) & (d): Ha signal, (b) & (e): TF coil current I_{TF} and PF1/PF7 coil current $I_{\mathrm{PF1/PF7}}$ and (c) & (f): measured partial pressure of hydrogen neutrals p_{neutral}.

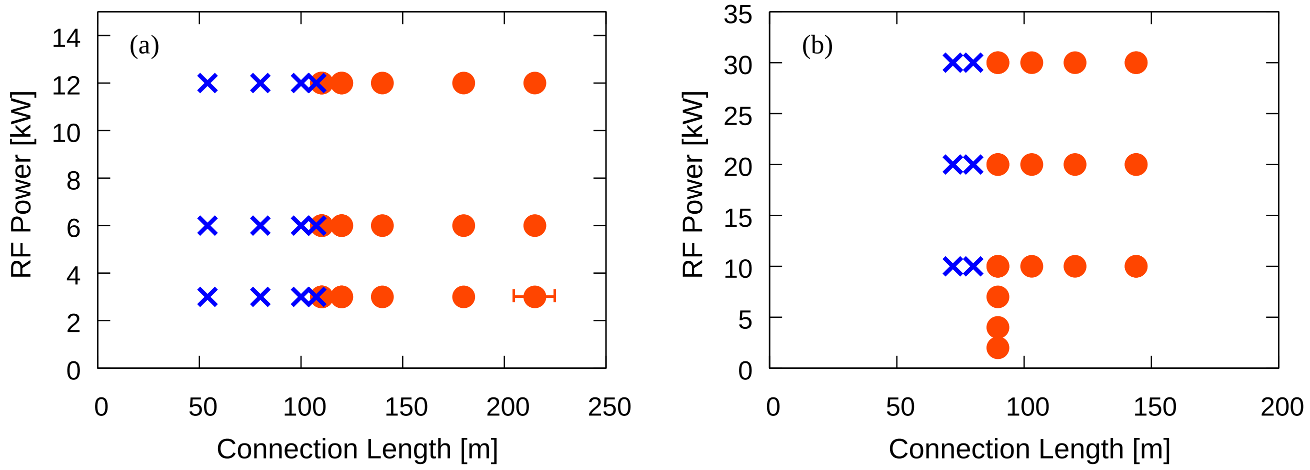

Fig. 6-2. Breakdown conditions with negative n-index, connection length vs RF power. (a) 2.45 GHz and (b) 8.2 GHz. Circle mark denotes where breakdown was obtained and cross does where it was not. For (b), error bar of L is sufficiently small: ±3 m.

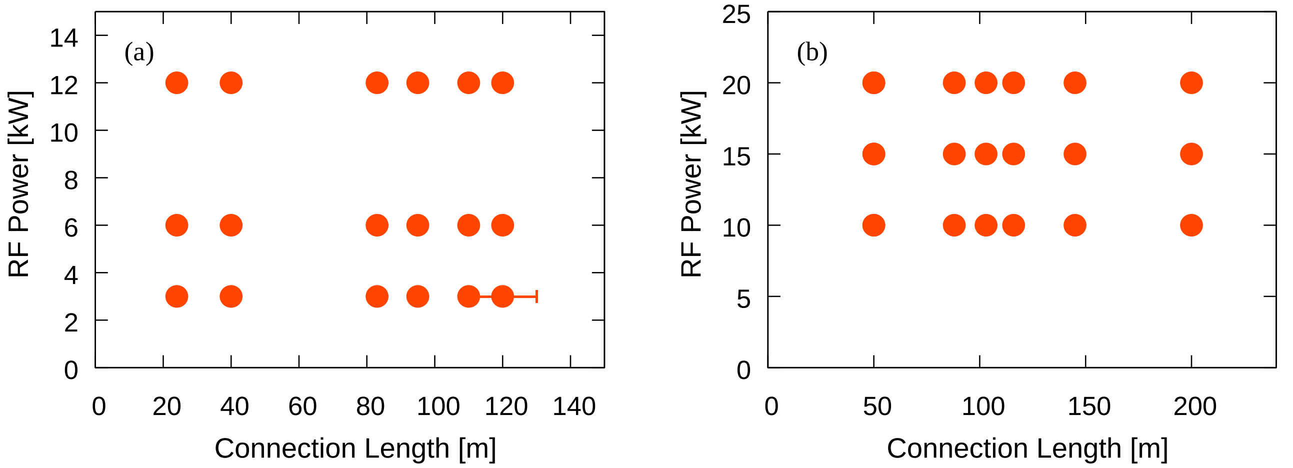

Fig. 6-3. Breakdown conditions with positive n-index, connection length vs RF power. (a) 2.45 GHz and (b) 8.2 GHz. There was no threshold for breakdowns with positive n-index in the experimental range. For (b), error bar of L is sufficiently small: ±3 m.

6.2 Analysis with One-point Model

From the experiments of RF-induced breakdown, we see that the lifetime of electrons plays an important role in QUEST experimental regime. Firstly, we look into the plasma parameters of electron temperature T_e and density n_e after breakdowns obtained for positive n-index. Typical distributions for positive n-index of T_e and n_e on the triple-probe array is shown in Fig. 6-4. In Fig. 6-4(a), T_e has a peak at R = 525 mm where it corresponds to the ECR layers. For 2.45 GHz and 8.2 GHz, ECR layers were located at R = 532 and 545 mm, respectively. A set of triple-probe has an inherent uncertainty of ±10 mm in the radial direction due to the layout of probe pins. T_e is an important parameter for breakdown because higher T_e enhances directly avalanche of electrons. In Fig. 6-4 (b), n_e shows a broad distribution around the ECR layer.

To evaluate the relationship between plasma parameters (T_e and n_e), connection length L and RF injection power, triple probes at R = 525 mm was selected, which represent breakdown conditions. For 2.45 GHz, dependence of T_e and n_e on L are denoted in Fig. 6-5. As for 8.2 GHz, it is shown in Fig. 6-6 in the same manner. In both frequencies, measured T_e is localized at R = 525 m. When we look at the dependence of T_e and n_e on L, there seems no dependence for both cases of 2.45 GHz and 8.2GHz. This is an evidence that L is not a primary factor for positive n-index configuration.

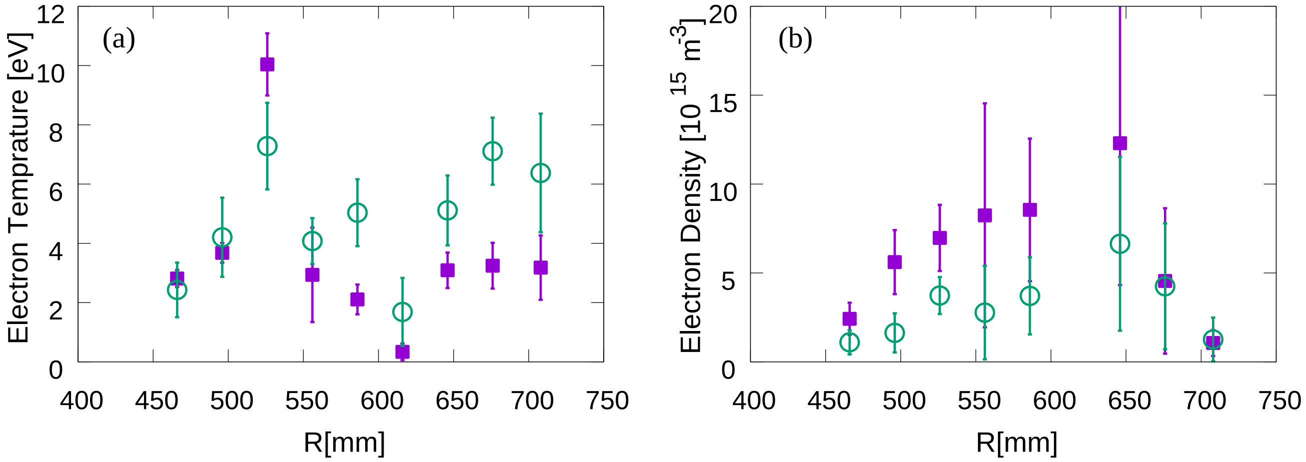

Fig. 6-4. Typical distribution for positive *n*-index of (a) T_e and (b) n_e by the triple probe array with 2.45 GHz and 8.2 GHz. RF power was set to 12kW and 10kW for 2.45 GHz and 8.2 GHz, respectively. For 2.45 GHz, $L \sim 220$ m and for 8.2 GHz, $L \sim 105$ m. Circle: 2.45 GHz and square: 8.2 GHz.

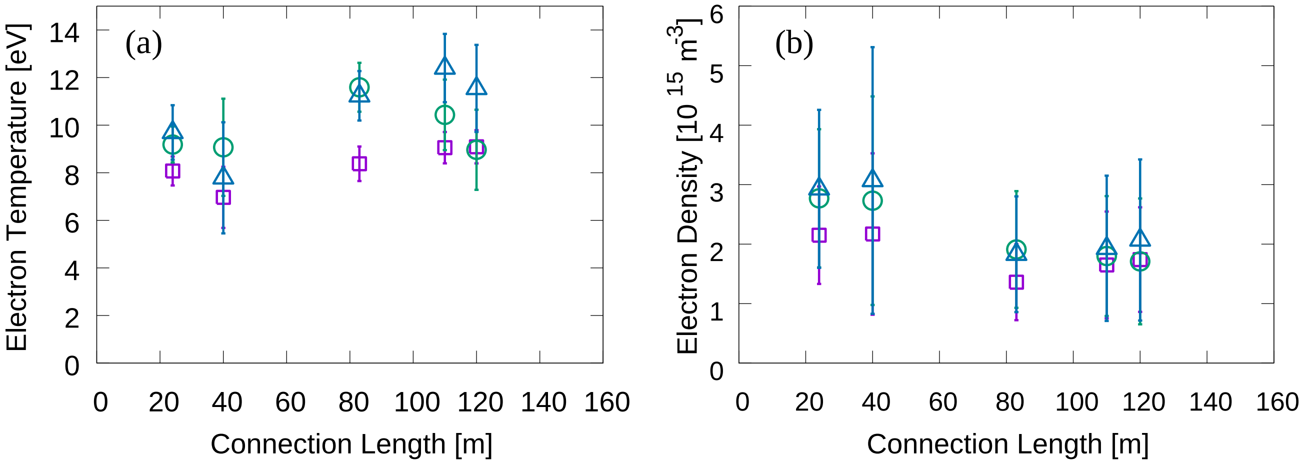

Fig. 6-5. Dependence on *L* for positive *n*-index with 2.45 GHz at $R = 525$ mm (a) T_e and (b) n_e. RF injection power, square: 2kW, circle: 6kW and triangular: 12kW.

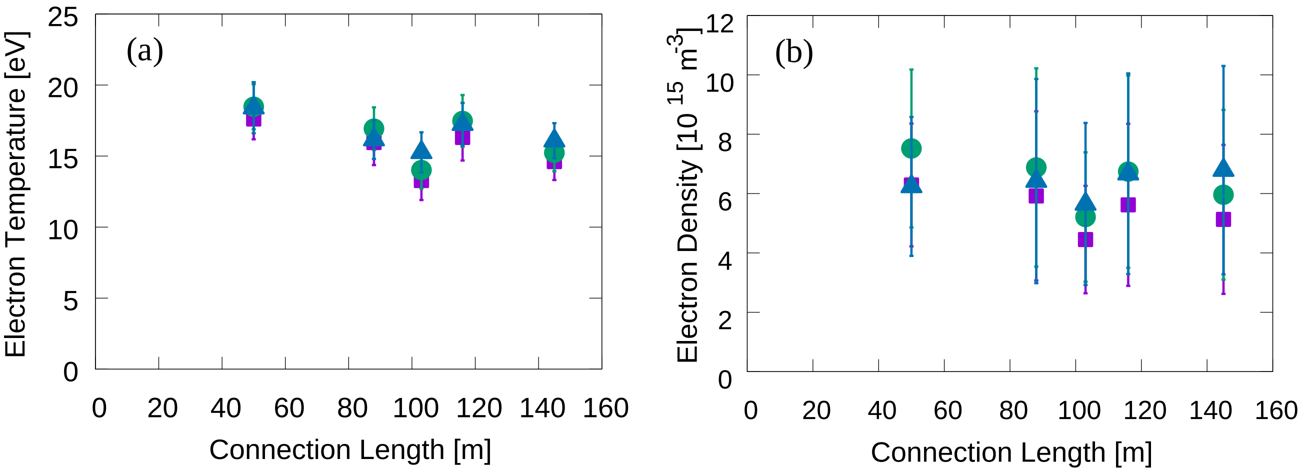

Fig. 6-6. Dependence on L for positive n-index with 8.2 GHz at $R = 525$ mm (a) T_e and (b) n_e. RF injection power, square: 10kW, circle: 15kW and triangular: 20kW.

For positive n-index, the electron lifetime, by which determines breakdown conditions, is difficult to estimate in the experiments because of the presence of confined electrons[3]. For that purpose, therefore, we start to consider the cases of negative n-index configuration that there are no confined electrons in the open field configuration. First, typical distributions for negative n-index of T_e and n_e on the triple-probe array is shown in Fig. 6-7. We also assume that the peak of T_e at R = 525 mm represents ECR layer and then we take values of triple probes at R = 525 and 555 mm. For 2.45 GHz, dependence of T_e and n_e on L are illustrated in Fig. 6-8, respectively. As for 8.2 GHz, it is also shown in Fig. 6-9. In comparison with positive and negative n-index configuration, we investigate the difference of T_e and n_e at the same frequency. First, as for 2.45 GHz, T_e at R = 525 mm stays in the same range with positive n-index: T_e = 7.0 ~ 12.0 eV in Fig. 6-5(a). However, it shows a linear dependence on L only with negative n-index that higher L forms plasma with higher T_e eV in Fig. 6-8(a). Meanwhile, when we compare the both n-index configurations, n_e stays in the same range and shows no dependence on L: n_e = 2.0 ~ 4.0×10^{15} m^{-3} (see Fig. 6-5(b) and Fig. 6-8(b)). Second, we look into the cases of 8.2 GHz. T_e at R = 525 mm becomes greatly larger with positive n-index (T_e = 15.0 ~ 20.0 eV in Fig. 6-6(a)) than that of negative n-index (T_e = 4.0 ~ 8.0 eV in Fig. 6-9(a)). Also in Fig. 6-9(a), with negative n-index, T_e shows a linear dependence on L as it is with 2.45 GHz. As for n_e profiles in comparison with Fig. 6-6(b) and Fig. 6-9(b), positive n-index forms higher n_e plasma. We can also observe a linear dependence of n_e on L that longer L is preferable for making higher n_e in Fig. 6-9(b). This can be explained simply that L is proportional to τ_{loss}, and higher n_e is required to constantly keep the loss term n_e/τ_{loss} in the equilibrium state, at which breakdown is achieved. Throughout the cases of positive and negative n-index, it is notable that higher injection power gives higher plasma parameters of T_e and n_e.

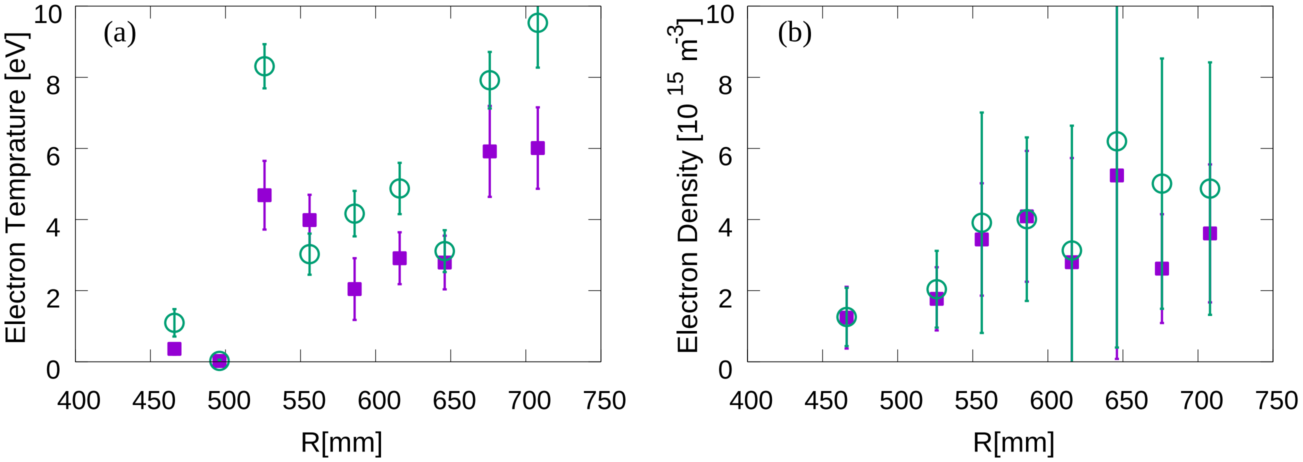

Fig. 6-7. Typical distribution for negative *n*-index of (a) T_e and (b) n_e by the triple probe array with 2.45 GHz and 8.2 GHz. RF power was set to 12kW and 10kW for 2.45 GHz and 8.2 GHz, respectively. For 2.45 GHz, $L \sim 220$ m and for 8.2 GHz, $L \sim 105$ m. Circle: 2.45 GHz and square: 8.2 GHz.

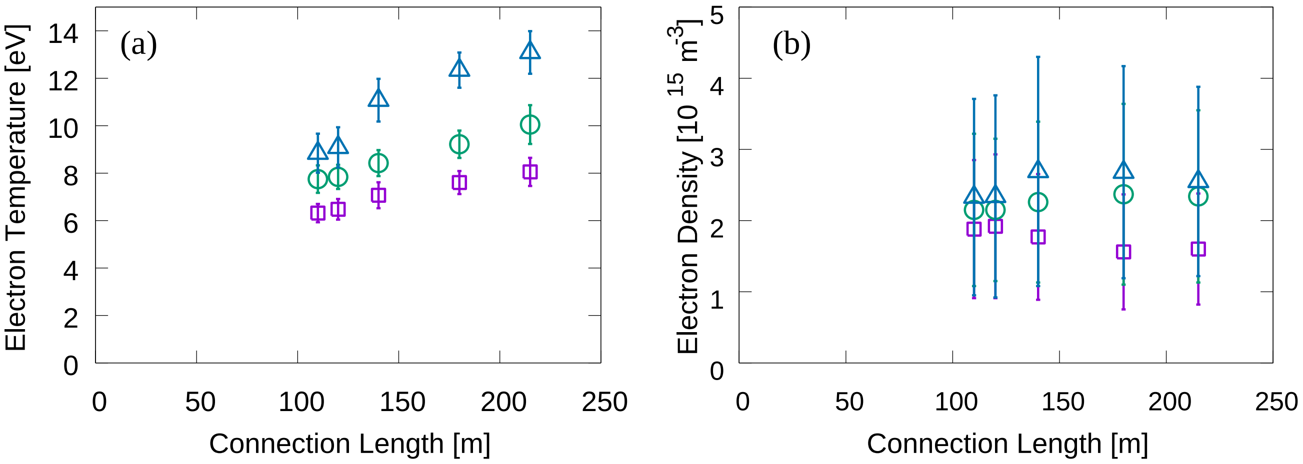

Fig. 6-8 Dependence on L for positive *n*-index with 8.2 GHz at $R = 525$ mm (a) T_e and (b) n_e. RF injection power, square: 2kW, circle: 6kW and triangular: 12kW.Circle: 2.45 GHz and square: 8.2 GHz.

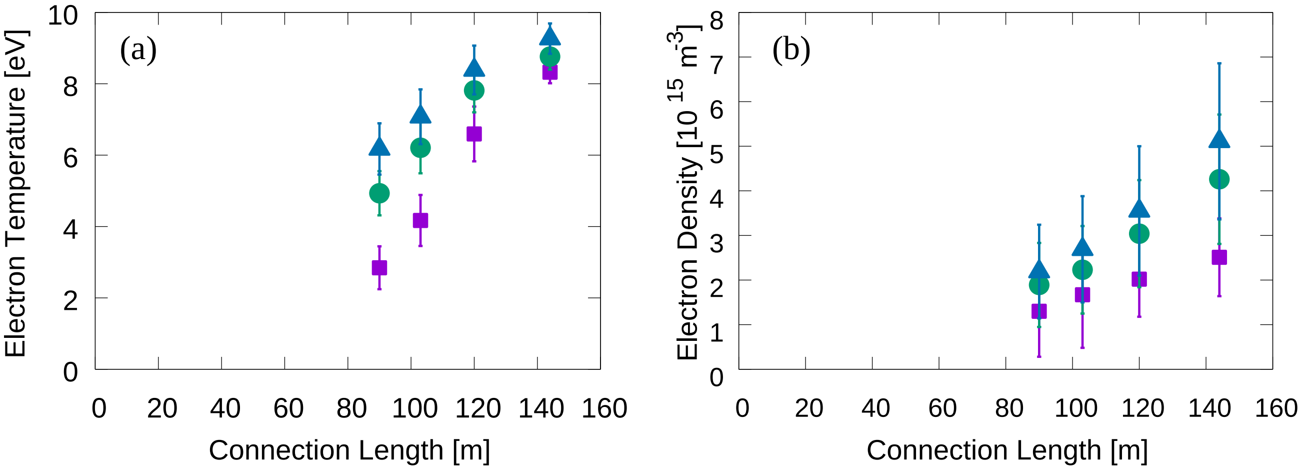

Fig. 6-9. Dependence on L for positive n-index with 8.2 GHz at $R = 525$ mm (a) T_e and (b) n_e. RF injection power, square: 10kW, circle: 15kW and triangular: 20kW.

In cases of negative *n*-index, where we have clear thresholds on *L* for RF-induced breakdown, a common observation for both frequencies of 2.45 GHz and 8.2 GHz is that T_e has a linear dependence on *L* in Fig. 6-8(a) and Fig. 6-9(a). The mechanism that there was no breakdown under the threshold can be explained as following. Since T_e decreases when *L* is shorter, we can expect that plasma heating by RF wave becomes inefficient under the threshold due to the superior electron loss, and required T_e for breakdown is not achieved. To verify this mechanism, calculations based on the developed one-point model were performed. In Fig. 6-10(a), we simulate when breakdown is obtained where *L* is above the threshold for both frequencies: $L = 120$ m. Other parameters are inserted based on experimental conditions: $T_e = 7.5$ eV and $n_e = 2.0\times10^{15}$ m^{-3} and $p_{\mathrm{neutral}} = 5.0\times10^{-3}$ Pa. In addition, a condition where no breakdown was observed is illustrated in Fig. 6-10(b): $L = 80$ m. For this condition with no breakdown, one can estimate the degree of T_e and n_e from its dependence on *L* (in Fig. 6-8 and Fig. 6-9). The estimated values are $T_e = 5.0$ eV and $n_e = 2.0\times10^{15}$ m^{-3}. When *L* is above the threshold ($L = 120$ m, Fig. 6-10(a)), the electron and hydrogen ion (H^+) density keeps growing until hydrogen molecule (H_2) as fuel is consumed (~0.025 sec). Therefore, this result corresponds to the conditions where breakdown was obtained in the experiments. That is, the production of plasma by electrons avalanche is superior to the loss along with magnetic lines of force. On the other hand, when *L* is shorter than the threshold ($L = 80$ m, Fig. 6-10(b)), electron and H^+ density decrease monotonically in time, and the initial n_e cannot be sustained. This results corresponds to the conditions that no breakdown was obtained. In this case, the electron loss due to magnetic lines of force is dominant compared with the ionization. Compared with the negative *n*-index experiments, the calculations in Fig. 6-10 show a good agreement that the thresholds of breakdown exist on $L = 110$ and 85 m for 2.45 GHz and 8.2 GHz, respectively. Here, as for 2.45GHz, *L* has an error range of ±20 m. Note that only initial values were inserted into the model but hydrogen neutrals were constantly inserted by mass flow meter in the experiments. Therefore, the evaluation of the model is valid only in the initial phase whether the plasma particle balance is enhanced or not. Since we focus on breakdown phase, particle loss after ECR plasma formation is not included in this study.

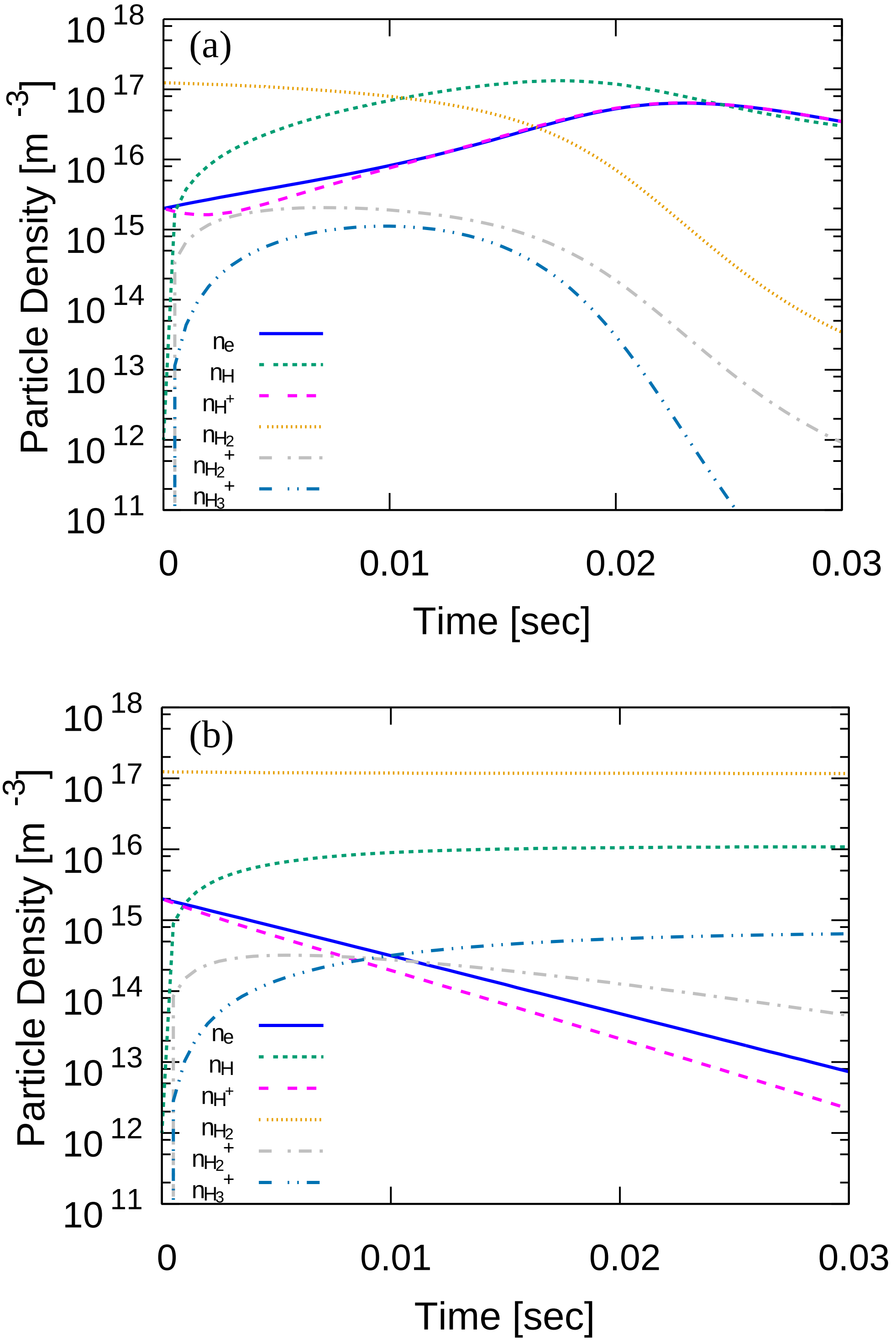

Fig. 6-10. One-point model calculation with the initial values: (a) $L = 80$ m, $T_e = 7.5$ eV, $n_e = 2.0\times10^{15}$ m^{-3} and $p_{\mathrm{neutral}} = 5.0\times10^{-3}$ Pa and (b) $L = 120$ m, $T_e = 5.0$ eV, $n_e = 2.0\times10^{15}$ m^{-3} and $p_{\mathrm{neutral}} = 5.0\times10^{-3}$ Pa.

In Fig. 6-10(a), the slope of n_e turns to negative value when reducing T_e, therefore we can search a minimum T_e required for breakdown. In Fig. 6-11, a comparison between the minimum T_e for breakdown from the model and experimental results of negative n-index at R = 525 mm are illustrated. Also, results of positive n-index at R = 525 mm for 2.45 GHz and 8.2 GHz are denoted to evaluate the difference in magnetic structure. From the model, the shorter L becomes; the higher T_e is required for breakdown. When L is shorter, an electron needs to ionize hydrogen neutrals with shorter distance. Then, higher T_e is required but at the same time the loss speed of electrons (C_s) becomes large. The modeling result is a consequence of these two conflicting factors. The two lines in Fig. 6-11(a) and 6-11(b) represent the range of change in p_{neutral} during the experiments ($p_{\mathrm{neutral}} = 3.0 \sim 6.0\times10^{-3}$ Pa). In Fig. 6-1(c), after several power modulations (breakdowns), the degree of p_{neutral} returns to the initial value. Furthermore, if there is no breakdown, p_{neutral} keeps constant during the shot duration. In this manner, we can assume that $p_{\mathrm{neutral}} \sim 5.0\times10^{-3}$ Pa is adaptable for breakdown phase. Note that higher p_{neutral} is preferable for breakdown in the experimental regime of QUEST since higher density of hydrogen neutrals enhances ionization of hydrogen by accelerated electrons. Firstly, for 2.45 GHz in Fig. 6-11(a), in comparison with modeling and experiments, it shows a good agreement with both positive and negative n-index. For T_e values with positive n-index, they are in the same range of negative n-index ($T_e = 8.0 \sim 12.0$ eV) where $L > 180$ m. This indicates that the lifetime of electrons with positive n-index with shorter L eventually becomes sufficient for breakdown. Meanwhile, T_e with negative n-index falls below the estimated minimum T_e around L = 100 m, and no breakdown was observed. Next, for 8.2 GHz in Fig. 6-11(b), measured T_e with negative n-index are slightly out of the modeling range at L = 85 m. From experimental values in Fig. 6-9(a), $T_e = 3.0 \sim 6.0$ eV, and from the modeling, $T_e >$ 7.0 eV is required. This may come from the experimental condition that the neutral pressure by ion gauge does not directly measure the value where breakdown takes place. Vacuum evacuation system during the experiments produces a flow of neutrals and makes it difficult to measure. As for positive n-index, measured T_e can be plotted sufficiently higher: $T_e = 15.0 \sim 20.0$ eV. In summary of Fig. 6-11, the model estimation of minimum T_e for RF-induced breakdown describes that required T_e increases as L becomes shorter related with the loss mechanism. This is consistent with the experimental results that T_e linearly falls as L approaches to the experimental thresholds. By the combination of experiment and modeling, minimum $T_e = 4.0 \sim 7.0$ eV can be estimated for RF-induced breakdown in the QUEST experimental regime.

In discussion, dependence on RF injection power was not obtained throughout experiments. The threshold of injection power supposed to exist in the range of few kW, however, precise control of injection power is difficult for the equipped system. In addition, only particle balance equations are taken into account in the present study. Therefore, to relate RF power to breakdown conditions, it is necessary to include energy balance equations[4]. Besides, the difference in two frequencies of 2.45 GHz and 8.2 GHz was not significant in the experiments and it stays in an error range such as L thresholds for breakdown and minimum T_e. However, in comparison of frequencies with negative n-index, obtained values of T_e are comparable despite the injection power is more than twice. Typically, 10 kW injection of 2.45 GHz: T_e = 9.0 ~ 13.0 eV, 20 kW injection of 8.2 GHz: T_e = 6.0 ~ 8.0 eV in Fig. 6-11. This may indicate ECR heating with lower frequency can efficiently couple power to electrons. This mechanism was also calculated theoretically as collision-less nonlinear absorption at ECR layer.

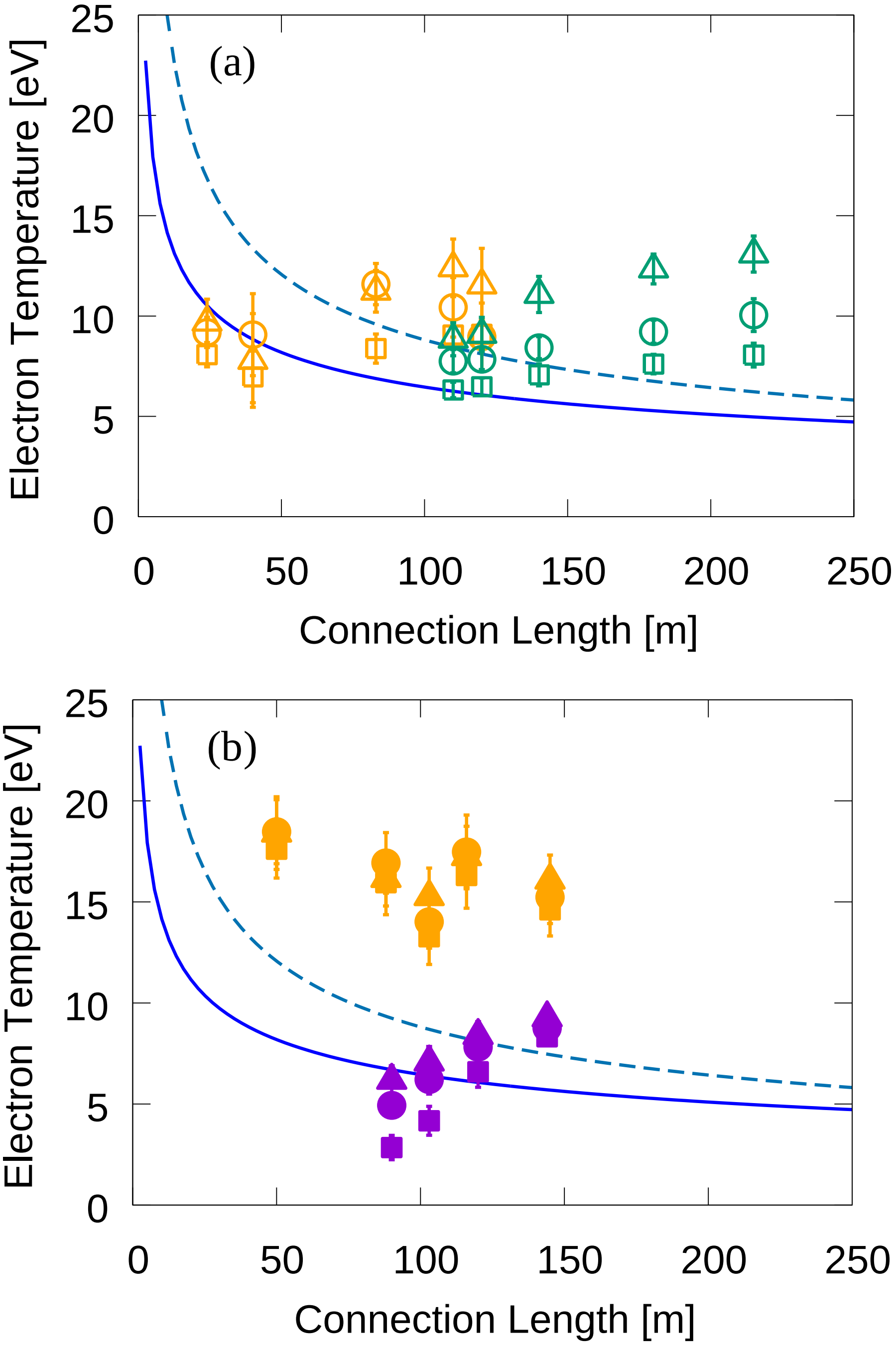

Fig. 6-11. Modeling results for the minimum T_e required for breakdown. Solid line with initial conditions of $n_{e0} = 2.0\times10^{15}$ m^{-3} and $p_{\mathrm{neutral}} = 6.0\times10^{-3}$ Pa. Dashed line with $n_{e0} = 2.0\times10^{15}$ m^{-3} and $p_{\mathrm{neutral}} = 3.0\times10^{-3}$ Pa. (a) experimental results for 2.45 GHz at R = 525 mm. Green marks: negative n-index. Orange marks: positive index. As for RF power, Square: 2kW, circle: 6kW and triangular: 12kW. (b) results for 8.2 GHz at R = 525 mm. Purple marks: negative n-index. Orange marks: positive n-index. For RF power, Square: 10kW, circle: 15kW and triangular: 20kW.

6.3 Second Harmonic ECR Breakdown

We also evaluate the difference in fundamental and second harmonics breakdown. With second harmonics ECR, negative *n*-index configuration could not make breakdowns so that we focus on positive *n*-index. The experiments were carried out with 8.2 GHz and 28GHz. In Fig. 6-12, the relation of RF injection power and obtained density is presented. In experiments, for 8.2, RF power below 60kW could not make breakdown. For 28GHz, the power threshold was about 150kW. Note that conditions for 28GHz were very sensitive for magnetic structure, showing that dependence on RF power is high. Compared to the fundamental ECR breakdown experiments, where minimum power requirements for 2.45GHz and 8.2GHz were less than few kW, second harmonics ECR is hardly to get breakdown. From the analysis of non-linear power absorption, which introduced in Chapter 3, we can evaluate frequency dependence. Figure 6-13 shows that lower frequency is easy to get higher electron temperature, which is consistent with experiments of fundamental and second harmonics ECR. It also shows that energy transfer rate of fundamental and second ECRH largely differs. Therefore, the condition of second ECR breakdown should highly depends on how much energy electrons can obtain not on the loss scheme.

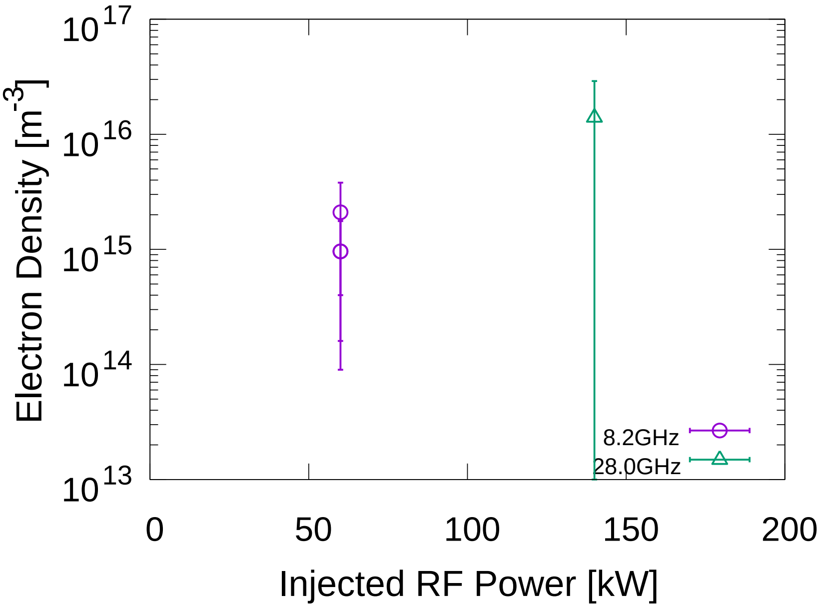

Fig. 6-12. RF injection power vs electron density after breakdowns.

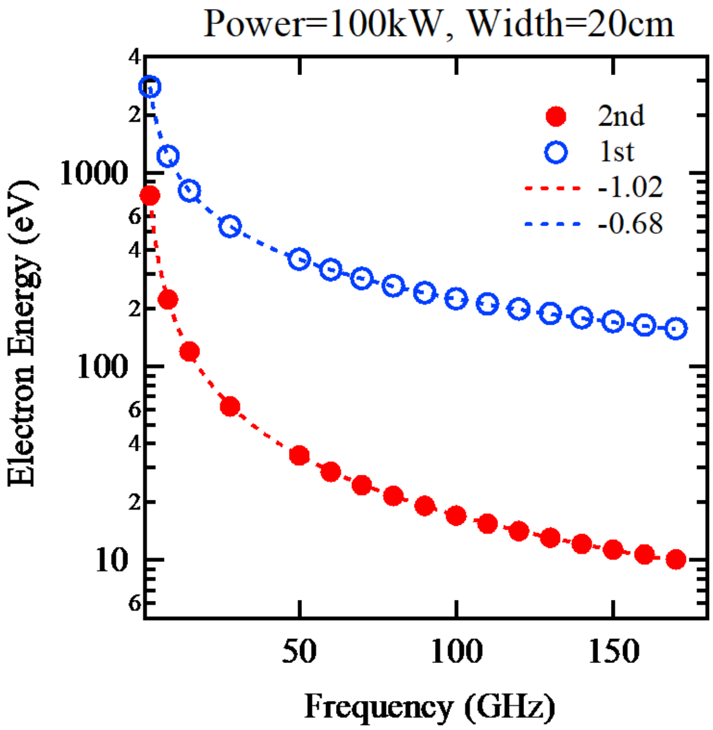

Fig. 6-13. Frequency dependence of fundamental and second ECRH. Vertical axis is the energy that one electron gained with one transit of ECR surface. Injection is X-mode. RF power is set to 100kW and half-width of RF to 20cm.

Refs in Chapter 6

[1] R. Yoneda, K. Hanada, K. Nakamura, H. Idei, N. Yoshida, M. Hasegawa, T. Onchi, K. Kuroda, S. Kawasaki, A. Higashijima, T. Nagata, A. Isayama, O. Mitarai, A. Fukuyama, and Y. Takase, Cit. Phys. Plasmas **24**, (2017).
[2] C.B. Forest, Y.S. Hwang, M. Ono, G. Greene, T. Jones, W. Choe, M. Schaffer, A. Hyatt, T. Osborne, R.I. Pinsker, C.C. Petty, L. J, and S. Lippmann, Phys. Plasmas **1**, 1568 (1994).
[3] M. Ishiguro, K. Hanada, H. Liu, R. Ogata, M. Isobe, S. Tashima, H. Zushi, K. Sato, A. Fujisawa, K. Nakamura, H. Idei, M. Sakamoto, M. Hasegawa, Y. Takase, T. Maekawa, Y. Kishimoto, O. Mitarai, S. Kawasaki, H. Nakashima, and A. Higashijima, J. Phys. Conf. Ser. **511**, 12041 (2014).
[4] T. Wauters, A. Lyssoivan, D. Douai, O. Marchuk, D. Wünderlich, R. Koch, G. Sergienko, G. Van Oost, and M. Van Schoor, Plasma Phys. Control. Fusion **53**, 125003 (2011).

7. Concluding Remarks

We have presented a combinative investigation of experiments in QUEST and the one-point point model of hydrogen ionization for RF-induced plasma breakdown. The experiments showed different behaviors with positive and negative *n*-index configurations of magnetic structures. In case of negative *n*-index, there existed a clear threshold on connection length *L* of magnetic lines of force with negative *n*-index in both frequencies of 2.45 GHz and 8.2 GHz. The result the electron temperature T_e only with negative n-index has a linear dependence on *L* denotes that RF heating becomes less effective as *L* decreases because the lifetime of electrons is only governed by *L* on which electrons escape. In contrast, in case of positive n-index configurations, breakdown was always attainable even *L* is shorter than the threshold for negative n-index. This indicates positive n-index is preferable for RF-induced breakdown, since the lifetime of electron becomes sufficiently longer by the presence of electron's closed orbit even in the open field. Positive *n*-index configuration is suitable for current start-up that it can also provide a magnetic flux to keep tokamak equilibrium after formation of closed magnetic surface. Start-ups on large superconducting tokamaks such as ITER should include this effect of confined electrons by RF for more reliable and cost-effective planning.

The one-point model of hydrogen ionizations, which employs electron's loss term defined by ambipolar diffusion along *L*, showed that the shorter *L* becomes; the higher T_e is required for breakdown. The experimental thresholds of *L* for breakdown showed an agreement with modeling results especially with 2.45 GHz. The combination of the experiments and modeling represented that the minimum electron temperature is predicted for RF-induced breakdown in tokamak magnetic structure.

We also take a consideration of second harmonic ECR breakdown experiments in QUEST. With the non-linear heating analysis, we have an agreement with experiments. First, required RF power for second ECR breakdown is very much higher than that of fundamental. Second, higher frequency ECR requires higher RF power for breakdown.

Future Works

1. For model development, introduction of energy balance equations are to be finished to realize self-consistent modeling of RF-induced breakdown. Estimation of power thresh hold is attainable.
2. In experiments, the threshold of minimum injection power for 2.45GHz and 8.2GHz have not been evaluated. Detailed investigation, including all frequencies in QUEST, is necessary and analysis from modeling side might be helpful.

8. Acknowledgments

I'd like to show an appreciation to my supervisor, Professor Kazuaki Hanada, for giving me his reliable instructions and opportunity to work with people all over the world. This Ph.D. work would have not been accomplished without his kindness and discreet understanding in plasma physics. Hope that we can continue to work together in fusion research.

Next, I'd like to give my gratitude to Professor Reiji Hattori, my supervisor during master course. Experiences that I learned in his laboratory helped me a lot when considering electronic circuits for measurements.

My special thanks go to Professor Masayuki Ono, Dr. Roger Raman and Dr. Nicola Bertelli, who helped me a lot during my staying at Princeton Plasma Physics Laboratory. Collaborations with them inspired me how important and exciting international cooperation is.

I express my thanks to QUEST members: Professor Kazuo Nakamura, Professor Hiroshi Idei, Assistant Professor Makoto Hasegawa, Assistant Professor Takumi Onchi and Dr. Kengoh Kuroda. Their suggestions on experiments and analysis were very useful.
Also, I show my appreciations to the technical staffs: Mr. Shoji Kawasaki, Ms. Aki Higashijima, Mr. Nagata Takahiro and Mr. Shun Shimabukuro.

Support from Green Asia Program Office has been really helpful for pursuing Ph.D. in different circumstances. Especially, Professor Yasuyuki Nakao gave me a good motivation and discussion on my research.

Special thanks to Dr. Tomoaki Hirakawa, my classmate in Chikushi Campus, for sharing experiences and knowledge on research and daily lives. I also appreciate future Dr. Hatem Elserafy in Hanada lab for giving me a lot of energy when I am down. Dr. Osamu Watanabe and Dr. Kotaro Yamasaki were always there when I have difficulty. Not enough space to mention but I really want to say thank you to everyone I met during my 5 years in Kyushu.

Finally, I would like to show my great thanks to my family for letting me do what I want for such a long time. Their generous understanding always gave me peace of mind.